Geoscience Frontiers 12 (2021) 101106

Contents lists available at ScienceDirect

Geoscience Frontiers

journal homepage: www.elsevier.com/locate/gsf

The western Durkan Complex (Makran Accretionary Prism, SE Iran): A Late Cretaceous tectonically disrupted seamounts chain and its role in controlling deformation style

Edoardo Barbero [a], Luca Pandolfi [b,c], Morteza Delavari [d], Asghar Dolati [d], Emilio Saccani [a,*], Rita Catanzariti [c], Valeria Luciani [a], Marco Chiari [e], Michele Marroni [b,c]

[a] Dipartimento di Fisica e Scienze della Terra, Università di Ferrara, Via Saragat 1, 44123 Ferrara, Italy
[b] Dipartimento di Scienze della Terra, Università di Pisa, Via S. Maria 53, 56126 Pisa, Italy
[c] Istituto di Geoscienze e Georisorse, CNR, Pisa, Via G. Moruzzi 1, 56124 Pisa, Italy
[d] Faculty of Earth Sciences, Kharazmi University, Shahid Mofatteh St. 43, Tehran, Iran
[e] Istituto di Geoscienze e Georisorse, CNR, Firenze, Via La Pira 4, 50121 Firenze, Italy

ARTICLE INFO

Article history:
Received 4 May 2020
Received in revised form 23 October 2020
Accepted 3 December 2020
Available online xxxx

Handling Editor: Inna Safonova

Keywords:
Tectonically disrupted seamounts
Makran
Late Cretaceous
Iran
Neo-Tethys

ABSTRACT

The Durkan Complex is a key tectonic element of the Makran accretionary prism (SE Iran) and it has been interpreted as representing a continental margin succession. We present here a multidisciplinary study of the western Durkan Complex, which is based on new geological, stratigraphic, biostratigraphic data, as well as geochemical data of the volcanic and meta-volcanic rocks forming this complex. Our data show that this complex consists of distinct tectonic slices showing both non-metamorphic and very low-grade metamorphic deformed successions. Stratigraphic and biostratigraphic data allow us to recognize three types of successions. Type-I is composed by a Coniacian – early Campanian pelagic succession with intercalation of pillow lavas and minor volcaniclastic rocks. Type-II succession includes a volcanic sequence passing to a volcano-sedimentary sequence with Cenomanian pelagic limestones, followed by a hemipelagic sequence. This succession is characterized by abundant mass-transport deposits. Type-III succession includes volcanic and volcano-sedimentary sequences, which are stratigraphically covered by a Cenomanian platform succession. The latter is locally followed by a hemipelagic sequence. The volcanic rocks in the different successions show alkaline geochemical affinity, suggesting an origin from an oceanic within-plate setting. Our new results indicate that the western Durkan Complex represents fragments of seamounts tectonically incorporated in the Makran accretionary wedge during the latest Late Cretaceous–Paleocene. We propose that incorporation of seamounts in the frontal prism caused a shortening of the whole convergent margin and possibly contributed to controlling the deformation style in the Makran Accretionary Wedge during Late Cretaceous–Paleocene times.

© 2020 Elsevier B.V. This is an open access article under the CC BY-NC-ND license (http://creativecommons.org/licenses/by-nc-nd/4.0/).

1. Introduction

The subduction complexes develop at convergent plate boundaries when crustal material is transferred between the subducting oceanic plate and the overlying plate (Davis et al., 1983; Moore et al., 1990; Charvet and Ogawa, 1994; Meneghini et al., 2009; Kusky et al., 2013; Festa et al., 2018). The architecture (e.g., size and shape) and the prevalent tectonic processes (i.e., accretion vs. erosion) in subduction complexes are dependent on the nature of the subducting oceanic plate (e.g., lithosphere formed at low or fast spreading ridges, thickness of the sedimentary cover, etc.), on the convergence rate, on the obliquity of the subducting plate with respect to the frontal prism, as well as on the thickness of subducted trench sediments (Marroni and Pandolfi, 2001; Clift and Vannucchi, 2004; von Huene et al., 2004a, 2004b; Stern, 2011; Malatesta et al., 2013; Festa et al., 2018; Barbero et al., 2020a). The development of the frontal prism can also be largely influenced by the subduction of seamounts, i.e. geographically isolated magmatic reliefs that can elevate on the seafloor from 100 m up to emerge above sea level, and whose origin is usually associated with mantle plumes (Morgan, 1971; Staudigel and Clague, 2010; Safonova and Santosh, 2014). In fact, the entering and accretion of a seamount in a subduction complex can produce a strong impact on the frontal prism and, more broadly, on the geometry of the entire convergent margin (Lallemand and Le-Pichon, 1987; von Huene and Lallemand, 1990; Dominguez et al., 1998; Vannucchi et al., 2006; Ruh, 2016). Thus, the identification of accreted seamounts in fossil accretionary wedges and the assessment of their features can provide insights for the

* Corresponding author.
E-mail address: sac@unife.it (E. Saccani).

https://doi.org/10.1016/j.gsf.2020.12.001
1674-9871/© 2020 Elsevier B.V. This is an open access article under the CC BY-NC-ND license (http://creativecommons.org/licenses/by-nc-nd/4.0/).

understanding the main tectonic processes working during the evolution of the convergent margins (Lallemand et al., 1989; Clift and Vannucchi, 2004; Vannucchi et al., 2006; Clarke et al., 2018). Despite their importance, few studies report subducted and/or accreted fossil seamounts (MacPherson, 1983; Isozaki et al., 1990; Corcoran, 2000; Shervais et al., 2005; Bagheri and Stampfli, 2008; Schnur and Gilbert, 2012; Bonnet et al., 2020a, 2020b). The diagnostic criteria to distinguishing remnants of fossils seamounts are: (i) the occurrence of alkaline OIB-type basalts overlain by shallow-marine carbonates, slope volcaniclastic/carbonatic rocks, and/or pelagic shale and chert; and (ii) the lack of continental-derived clastic sediments (Isozaki et al., 1990; Isozaki, 1997; Safonova and Santosh, 2014; Safonova et al., 2016).

The Makran Accretionary Prism (SE Iran, Fig. 1a) is one of the best exposed accretionary prisms in the world whose origin is related to

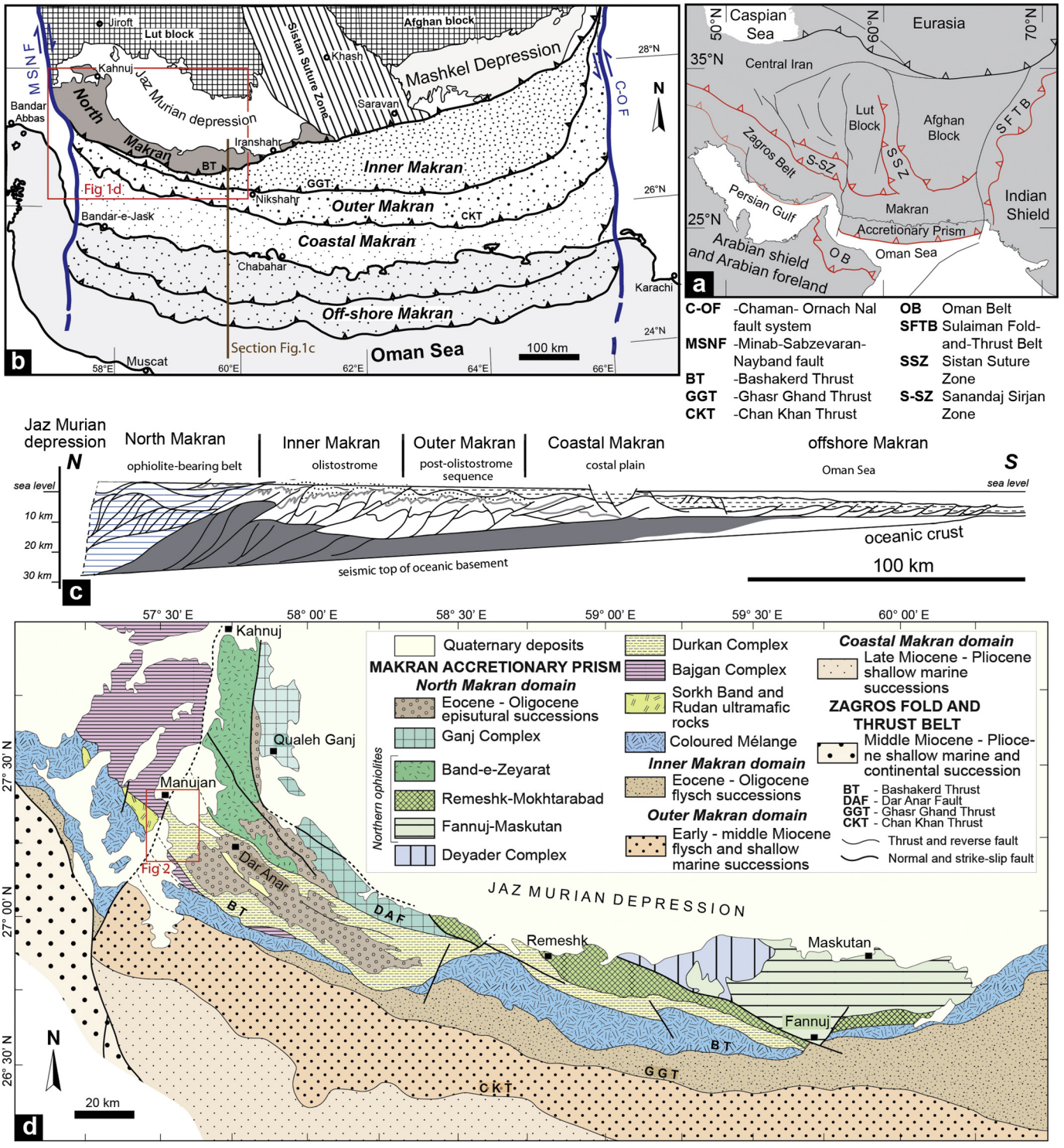

Fig. 1. Tectonic sketch map of the Iranian-Afghan-Pakistani area (a) showing the main tectonic subdivision (modified from Bagheri and Stampfli, 2008; Zanchetta et al., 2013; Mohammadi et al., 2016; Barbero et al., 2020b; Pirnia et al., 2020); structural sketch map (b) and related geological section (c) of the Makran Accretionary Wedge showing the different tectono-stratigraphic domain (modified from Burg et al., 2013); (d) simplified geological-structural map of the North Makran Domain showing the different tectonic unit (modified from Eftekhar-Nezhad et al., 1979; Samimi Namin, 1982, 1983; Burg, 2018; Barbero et al., 2020b).

the long-lived and complex geodynamic evolution of the Neo-Tethys Domain (McCall and Kidd, 1982; Burg, 2018). The complex geodynamic evolution of this area is mainly dominated by the northward subduction of the Neo-Tethyan oceanic lithosphere below the Lut and the Afghan blocks, which started from the Cretaceous and it is still active (Dercourt et al., 1986; Glennie et al., 1990; Barrier et al., 2018; Burg, 2018; Saccani et al., 2018). In the general framework of the Makran Accretionary Prism, the North Makran domain is characterized by the occurrence of several tectonic units and mélanges, in which oceanic magmatic rocks are widely preserved (Fig. 1b, c).

The Durkan Complex is one of the major tectonic elements of the North Makran and it includes a highly deformed assemblage mainly consisting of shallow water deposits associated with volcanic rocks, in some case slightly metamorphosed (McCall, 1985). This Complex is commonly interpreted as the sedimentary cover of the Bajgan Complex that, in turn, is regarded as an early Paleozoic or older continental basement (McCall and Kidd, 1982; Samimi Namin, 1983; McCall, 1985; Hunziker, 2014; Hunziker et al., 2015; Burg, 2018). This interpretation of the Bajgan and Durkan complexes has been suggested in most of the geodynamic reconstructions, which proposed the occurrence of a continental microplate separated from the Lut Block throughout a Late Jurassic–Early Cretaceous rifting stage (McCall and Kidd, 1982; McCall, 2002). Despite its importance for the geodynamic reconstruction of the Makran area, most of the studies on the Durkan Complex date back to more than thirty-five years ago (McCall, 1985). In addition, recent contributions (Hunziker, 2014; Hunziker et al., 2015) are largely based on previous geological interpretations. Up to now, no detailed stratigraphic reconstruction, no geochemical data on volcanic rocks, and very scarce biostratigraphic data are available in literature.

In this paper we present new geological, stratigraphic, and biostratigraphic data on the sedimentary and meta-sedimentary successions as well as new geochemical data on the associated volcanic and meta-volcanic rocks cropping out in the western sector of the Durkan Complex (i.e., in the Manujan area, Figs. 1d and 2). The aim of this study is to define the stratigraphic succession and the age of the sedimentary and volcanic sequences of the Durkan Complex in the Manujan sector. New findings allow us to propose that, in contrast to previous interpretations, the Durkan Complex represents a Late Cretaceous dismembered seamount or, eventually part of seamounts chain.

2. Geological setting

2.1. The Makran Accretionary Prism

The Makran Accretionary Prism results from the Cretaceous to Present-day convergence between the Arabian and the southern margin of Eurasian plates. This convergence was associated with northward subduction of the Neo-Tethys Ocean below the Eurasia margin (McCall and Kidd, 1982; Platt et al., 1985; Dercourt et al., 1986; Ricou, 1994; Burg, 2018; Saccani et al., 2018; Monsef et al., 2019). Subduction of oceanic lithosphere of the Oman Sea is still active in the Makran (Fig. 1a–c) as indicated by both geophysical data (White and Klitgord, 1976; Kopp et al., 2000; Grando and McClay, 2007; Entezar-Saadat et al., 2017; Motaghi et al., 2020) and earthquake focal mechanisms (Engdahl et al., 2006; Penney et al., 2017). The Makran is an E–W trending accretionary wedge that is bounded by two N-S trending major strike-slip fault systems (Fig. 1a and b). It is separated from the Zagros fold-and-thrust belt (to the west) by the dextral Zendan-Minab

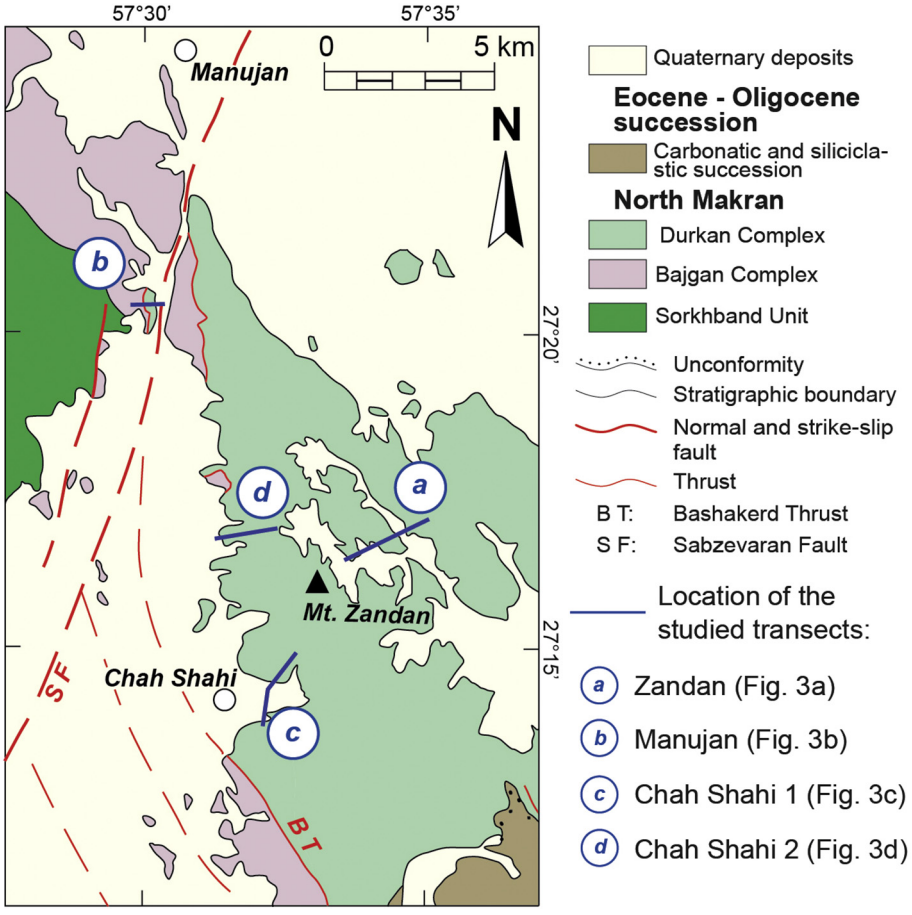

Fig. 2. (a) Simplified geological map of the Manujan sector showing the location of the studied transect (based on Samimi Namin, 1982 and modified according to our original fieldwork and photointerpretation with satellite images).

faults system and from the Himalaya continent-continent collision zone (to the east) by the sinistral Chaman-Ornach-Nal faults system (Kopp et al., 2000; Regard et al., 2010; Penney et al., 2015; Riaz et al., 2019)

The Makran Accretionary Prism includes an active, southernmost offshore wedge and an exhumed onshore prism (Fig. 1b and c). The onshore prism includes four major tectono-stratigraphic domains (Fig. 1b and c), which are, from the structural top to the bottom (i.e., from north to south): (i) the North Makran; (ii) the Inner Makran; (iii) the Outer Makran; (iv) the Coastal Makran (Dolati, 2010; Burg et al., 2013). These domains are tectonically juxtaposed through regional-scale and N-dipping thrust zones, showing progressively younger ages toward the south (Bashakerd, Ghasr Ghand and Chan Khan thrusts; Fig. 1b; see also Dolati, 2010; Burg et al., 2013; Dolati and Burg, 2013). The Bashakerd thrust (Fig. 1b) is a mainly E–W striking regional scale fault zone separating southward the North Makran from the Eocene–present day accretionary complex, which is represented by the Inner, Outer and Coastal Makran (Burg et al., 2013; Burg, 2018). The North Makran consists of an imbricate stack of both metamorphic and non-metamorphic continental and oceanic units (McCall and Kidd, 1982; Burg, 2018). These stacks were formed during the pre-Eocene geodynamic history of the Makran Accretionary Prism, as constrained by the unconformable deposition onto this domain of lower Eocene deposits (Samimi Namin, 1982; McCall, 1985, 1997, 2002). In contrast, the Inner, Outer and Coastal Makran domains include Eocene to Pleistocene mainly siliciclastic sedimentary successions that have been progressively incorporated in the frontal part of the accretionary prism (Platt et al., 1985; Burg et al., 2008, 2013; Dolati, 2010; Mohammadi et al., 2016; Burg, 2018).

2.2. The North Makran tectono-stratigraphic domain

The North Makran tectono-stratigraphic domain has been subdivided into several major tectonic units (Fig. 1d) bounded by either high angle faults or low angle shear zones (Eftekhar-Nezhad et al., 1979; Samimi Namin, 1983; McCall, 1985). These are from the north to the south and from the uppermost to the lowermost unit (Fig. 1d): (i) the Ganj Complex; (ii) the North Makran Ophiolites (Inner Makran Spreading Zone of McCall and Kidd, 1982); (iii) the Bajgan and Durkan Complexes; (iv) the Deyader Metamorphic Complex; (v) the Sorkhband – Rudan tectonic slices; (vi) the Coloured Mélange (Imbricate Zone of Burg et al., 2013).

The Ganj Complex has classically been included within the North Makran Ophiolites (McCall, 1985, 2002). However, this complex has recently been re-interpreted as representing the remnants of a Late Cretaceous volcanic-arc sequence, which was likely built up close to the southern margin of the Lut Block (Barbero et al., 2020b).

The North Makran ophiolites (Fig. 1d) include the Band-e-Zeyarat (Kananian et al., 2001; Ghazi et al., 2004; Barbero et al., 2020c), Remeshk-Mokhtarabad (McCall and Kidd, 1982; McCall, 2002; Hunziker, 2014; Burg, 2018), and Fannuj-Maskutan units (Desmons and Beccaluva, 1983; Moslempour et al., 2015; Sepidbar et al., 2020). All these ophiolites show Early Cretaceous and Late Cretaceous age and they are characterized by magmatic rocks mostly showing enriched-type mid-ocean ridge basalts (*E*-MORB) geochemical affinity and supra-subduction zone geochemical affinity, respectively (Desmons and Beccaluva, 1983; Ghazi et al., 2004; Burg, 2018; Monsef et al., 2019; Sepidbar et al., 2020). These ophiolitic units are considered as remnants of the North Makran Ocean (McCall and Kidd, 1982; Burg, 2018). In turn, it has been interpreted as either an Early Cretaceous back-arc basin related to the northward dipping subduction of the Neo-Tethys (McCall and Kidd, 1982) or a marginal basin opened during Late Jurassic–Early Cretaceous times along the southern margin of the Central Iran Block (Hunziker et al., 2015; Burg, 2018). Regardless of these different interpretations, it is commonly suggested that the opening of this basin led to the rifting of a microcontinental block (the so called Bajgan-Durkan microcontinent) from the Lut Block (McCall and Kidd, 1982; McCall, 2002; Hunziker et al., 2015; Burg, 2018).

The Bajgan and Durkan Complexes are regarded as a narrow (~40 km wide) block with continental affinity (Fig. 1d). Some authors suggested that the Bajgan and Durkan Complexes represent the southeastward continuation of the Sanandaj-Sirjan Zone (McCall and Kidd, 1982; McCall, 1985). However, these two complexes are characterized by completely different rock assemblages. The Bajgan Complex is an assemblage of metamorphic rocks that includes schists, paragneisses, amphibolites, and marbles, as well as basic and acidic meta-intrusive rocks and rare glaucophane-bearing schists (McCall, 1985; McCall, 2002; Dorani et al., 2017). The tectono-metamorphic evolution and the age of this complex is poorly known. McCall (1985) and Dorani et al. (2017) estimated metamorphic conditions characterized by a moderately high pressures and relatively high temperatures. In contrast, the Durkan Complex is non metamorphic or slightly metamorphic (i.e., from diagenetic condition to subgreenschist facies) and it has been considered as the original sedimentary cover of the metamorphic Bajgan Complex (McCall, 1985, 2002). The Durkan Complex consists of an assemblage of tectonic slices showing different stratigraphic successions, including: (i) Lower Cretaceous to Paleocene shallow-water limestones and thick sequences of alternating limestones, sandstones, shales, cherts, volcanics and volcaniclastics; (ii) rare tectonic slices of Carboniferous, Permian, and Jurassic shelf carbonate rocks, and (iii) subordinate marbles and schists (McCall, 1985, 2002; Hunziker et al., 2015). In addition, different types of granitoids have been intruded into Permian and Jurassic shelf limestones in the eastern sector of the Durkan Complex (Hunziker et al., 2015; Burg, 2018). They progressively range from Early Jurassic granites to Middle–Late Jurassic diorite-trondhjemite-plagiogranite suite. According to Hunziker et al. (2015), this lithological variation records the chemical evolution of the different magmatic pulses associated with the extensional tectonics of the southern margin of the Central Iranian Block, which led to the Late Jurassic–Early Cretaceous opening of the North Makran Ocean.

The Deyader Metamorphic Complex out crop in the eastern sector of the North Makran (Fig. 1d). It is a metamorphic complex showing High Pressure-Low Temperature (HP-LT) metamorphism and consisting of meta-limestones, meta-volcanics and meta-gabbros affected by HP-LT metamorphism (Delaloye and Desmons, 1980; McCall, 1985; Hunziker et al., 2015; Omrani et al., 2017).

The Coloured Mélange consists of an assemblage of lozenge-shaped, metric- to decametric-thick slices that includes volcanic rocks, cherts, limestones, serpentinites, gabbros, shales, as well as various types of metamorphic rocks, such amphibolites and HP-LT meta-basalts (Gansser, 1955; McCall, 1983, 2002; Saccani et al., 2018; Esmaeili et al., 2019, 2020). The formation of the Coloured Mélange was associated with the Cretaceous subduction of the Neo-Tethys ocean and it includes a great variety of volcanic rocks from both the subducting oceanic plate and the overidding plate (Saccani et al., 2018). Remnants of the subducting plate consist of Late Cretaceous oceanic plateau basalts, normal-type mid-ocean ridge basalts (N-MORB), and alkaline within-plate basalts (OIB). Moreover, remnants of the upper plate include Early to Late Cretaceous island arc tholeiites and calc-alkaline basalts likely formed in a forearc-arc tectonic setting. McCall (2002) and Saccani et al. (2018) suggested a late Paleocene age of formation for this mélange.

The Sorkhband and Rudan tectonic slices crop out between the Coloured Mélange and the Bajgan Complex (McCall, 2002; Delavari et al., 2016). They consist of slices of ultramafic and mafic rocks, up to 4 km thick. The Sorkhband tectonic slice includes gabbros derived from a mid-ocean ridge tectonic setting tectonically juxtaposed to mantle peridotites and lower crust rocks generated at a supra-subduction zone setting (Delavari et al., 2016). A Jurassic or Late Cretaceous age has been proposed for these rocks by Delavari et al. (2016).

3. The Durkan Complex in the western North Makran

3.1. General field features

The Durkan Complex defines a NW-SE striking tectonic element, which is bounded by regional-scale fault zones (Fig. 1d). To the north, the high angle and north dipping Dar-Anar Fault juxtaposes, with reverse kinematic, the Band-e-Zeyarat ophiolites and the Ganj Complex onto the Durkan Complex (Fig. 1d). To the south, the deformation zone related to the Bashakerd thrust juxtaposes the Durkan Complex onto the Bajgan Complex, the Coloured Mélange, and the Inner Makran turbiditic sequences (Fig. 1d). In the neighbourhood of Manujan, both the Durkan Complex and the Bashakerd thrust are abruptly truncated by the NNE-striking dextral Sabzevaran Fault (Figs. 1d and 2). The Durkan Complex consists of an assemblage of distinct fault-bounded slices (Fig. 3a–d). These slices are characterized by stratigraphic successions deformed by polyphase folding and thrusting phases (Fig. 4). In addition, several tectonic slices exhibit various tectono-metamorphic overprints, which range from anchizonal facies to subgreenschist facies. The thickness of the successions in the different tectonic slices is difficult to be constrained in detail due to the isoclinal folds duplicating the stratigraphic succession (Fig. 4). Nonetheless, their thickness can generally be estimated as at least several hundreds of metres.

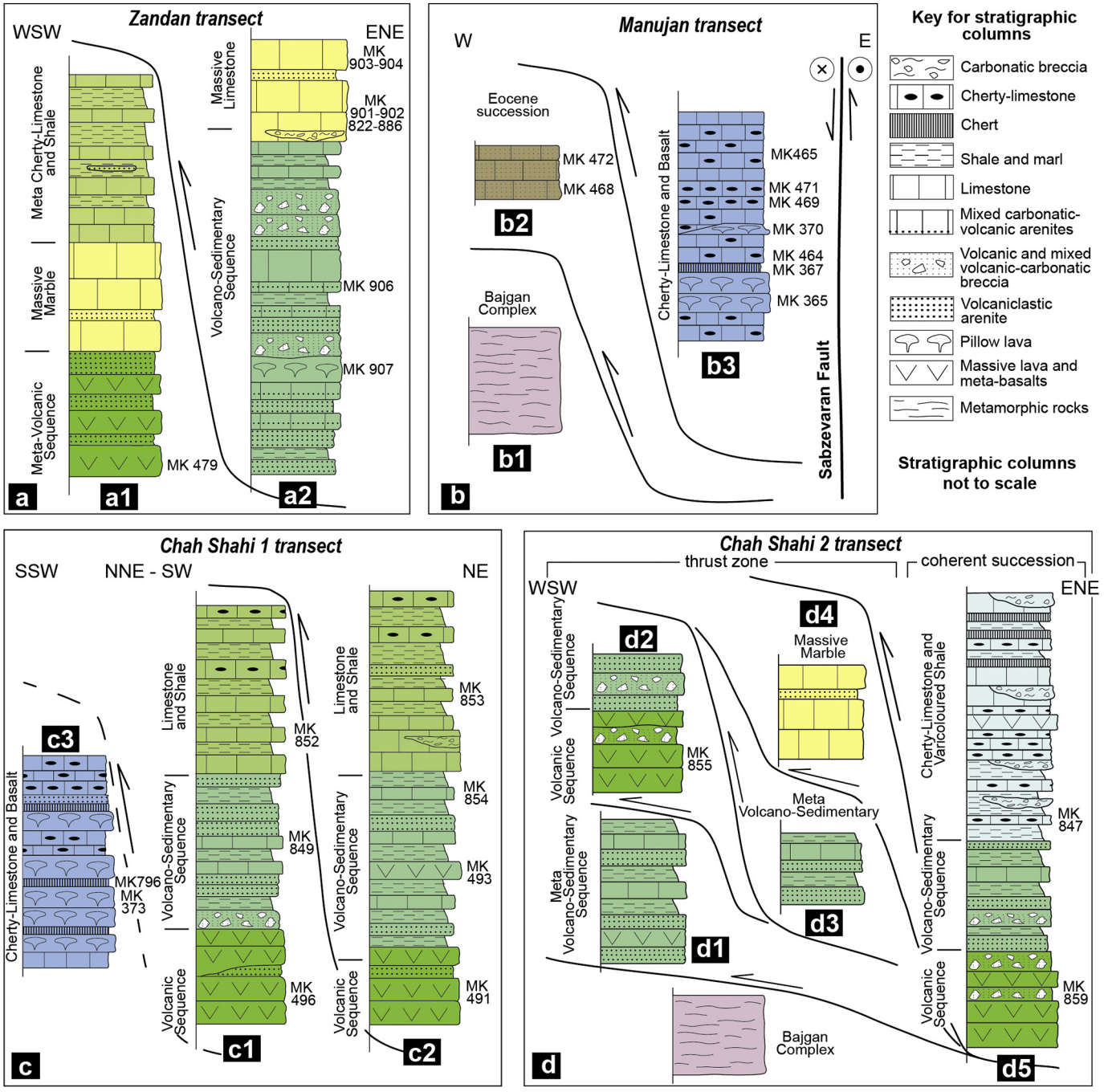

Fig. 3. Schematic stratigraphic-structural setting and stratigraphic columns for the successions in the studied transects: Zandan transect (a), Manujan transect (b), Chah-Shahi 1 transect (c), and Chah-Shahi 2 transect (d). Location of the transects are shown in Fig. 2.

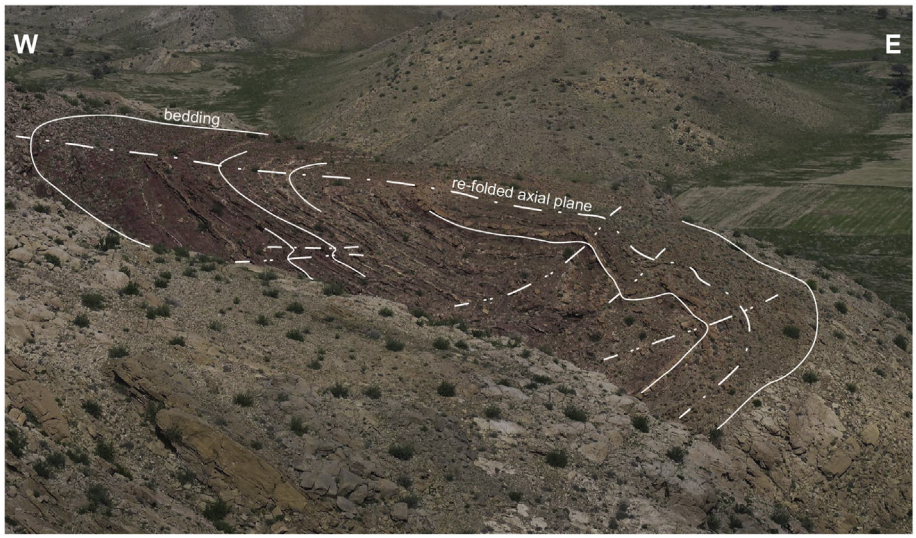

Fig. 4. Panoramic view of the polyphase folding deformation of the Durkan Complex successions showing W-verging isoclinal fold re-folded by *E*-verging open folds (axial planes and bedding are indicated in this figure).

This complicated structural setting resulted from multiple deformation stages, which occurred during the long-lived tectonic evolution of the Makran Accretionary Prism (McCall, 1985). In fact, the unconformable deposition of early Eocene successions onto the deformed and folded Durkan Complex (Figs. 1d and 2) indicates that this complex has been deformed during the pre-Eocene tectonic evolution of the North Makran (see also McCall, 1985, 2002). In addition, McCall (1985) suggested that the present-day structural setting of the Durkan Complex also resulted from the post-Eocene deformative stages. A detailed structural analysis and discussion of the structural evolution of the Durkan Complex is beyond the scope of this paper. Therefore, the general structural relationship among the different tectonic slices will be discussed. The tectono-stratigraphic architecture of the Durkan Complex will be investigated in detail by focusing on four key transects in which different stratigraphic successions are well preserved within distinct tectonic slices (Figs. 2 and 3).

3.2. Tectono-stratigraphic architecture

3.2.1. The Zandan transect

This transect is located to the east of the Mt. Zandan (Fig. 2). Here, two tectonic slices are juxtaposed through an ENE-dipping medium-to-high angle reverse shear zone. They display different stratigraphic successions, as schematically shown in Fig. 3a. The succession of the lower unit has been metamorphosed under subgreenschist facies conditions. It consists of a Meta-Volcanic Sequence passing upward to a carbonatic meta-sedimentary succession; the latter can be further subdivided into two lithostratigraphic units, namely: the Massive Marble and the Meta Cherty-Limestone and Shale (Fig. 3a1). The Meta-Volcanic Sequence show primary stratigraphic relationships with the Massive Marble and it is characterized by massive meta-volcanic rocks (Fig. 5a). These are alternated with coarse- and fine-grained meta-volcanoclastic arenites (Fig. 5b). Meta-volcanic rocks exhibit millimetre-spaced foliation characterized by fine-grained chlorite, epidote, actinolitic amphibole and minor albite. The Meta-Volcanic Sequence passes upward to the Massive Marble (Figs. 3a1 and 5a). The succession of the Massive Marble lithostratigraphic unit consists of massive whitish to yellowish marbles (Fig. 5a, c). Medium to thin beds of greenish meta-volcanoclastic arenites are locally interbedded within the marbles, suggesting primary stratigraphic relationships between the Massive Marble and the Meta-Volcanic Sequence (Figs. 3a1 and 5d). The upper part of the meta-sedimentary succession consists of the Meta Cherty-Limestone and Shale (Fig. 3a1). This lithostratigraphic unit is made up of medium to thin beds of whitish to pinkish meta cherty-limestone and marble alternating with shaly marls, varicoloured shales (Fig. 5e), brownish- to yellowish meta-limestones, and subordinate meta-volcaniclastic arenites. The succession of the Meta Cherty-Limestone and Shale shows an upward thinning of the meta-limestone beds coupled with the increase in abundance of the shales, shaly-marls, and brownish meta-limestones (Fig. 3a1).

Although the stratigraphic succession of the upper tectonic slice shows intense folding and deformation, no metamorphic recrystallization can be observed and the primary sedimentary features are fairly well preserved. This succession includes two distinct lithostratigraphic units: the Volcano-Sedimentary Sequence and the overlying Massive Limestone (Fig. 3a2). The Volcano-Sedimentary Sequence is characterized by pillow lava flows and volcanic breccia (Fig. 5f) alternating with different types of sedimentary rocks. The pillow basalts commonly show amygdaloidal texture, characterized by rounded-shaped vesicles filled by calcite, and chlorite. Locally, pluri-centimetric limestone clasts are enclosed within the volcanic breccia, suggesting that the volcanic activity was coeval with the carbonatic sedimentation. The volcanic rocks are subordinate in volume and are interbedded within a sedimentary succession. This succession is mainly made up of volcanoclastic arenites (Fig. 5g) and calcareous turbidites alternating with greenish fine-grained shales. The calcareous turbidites display framework composition characterized by both carbonatic and volcanic lithic fragments, as well as bioclast fragments, indicating a mixing between two distinct components. Lenticular-shaped massive limestones are intercalated at different stratigraphic levels within the Volcano-Sedimentary Sequence (Figs. 3a2 and 5h). This, again, indicates coeval volcanic activity and carbonatic sedimentation. The transition between the Volcano-Sedimentary Sequence and the overlaying Massive Limestone succession is marked by alternating levels of shale and cherty limestone and, locally, by massive, lenticular bodies of carbonatic megabreccia (Fig. 3a2). The latter consists of sub-angular to rounded clasts of fossiliferous limestones embedded within a fine-grained greyish carbonatic matrix (Fig. 5i). The Massive Limestone succession (Fig. 5h) consists of alternating grainstones, packstones and minor mudstones. The coarse-grained limestone varieties are characterized by abundant benthic foraminiferal bioclasts and green algae fragments set within a fine-grained recrystallized/micritic matrix indicating a shallow-water platform depositional environment.

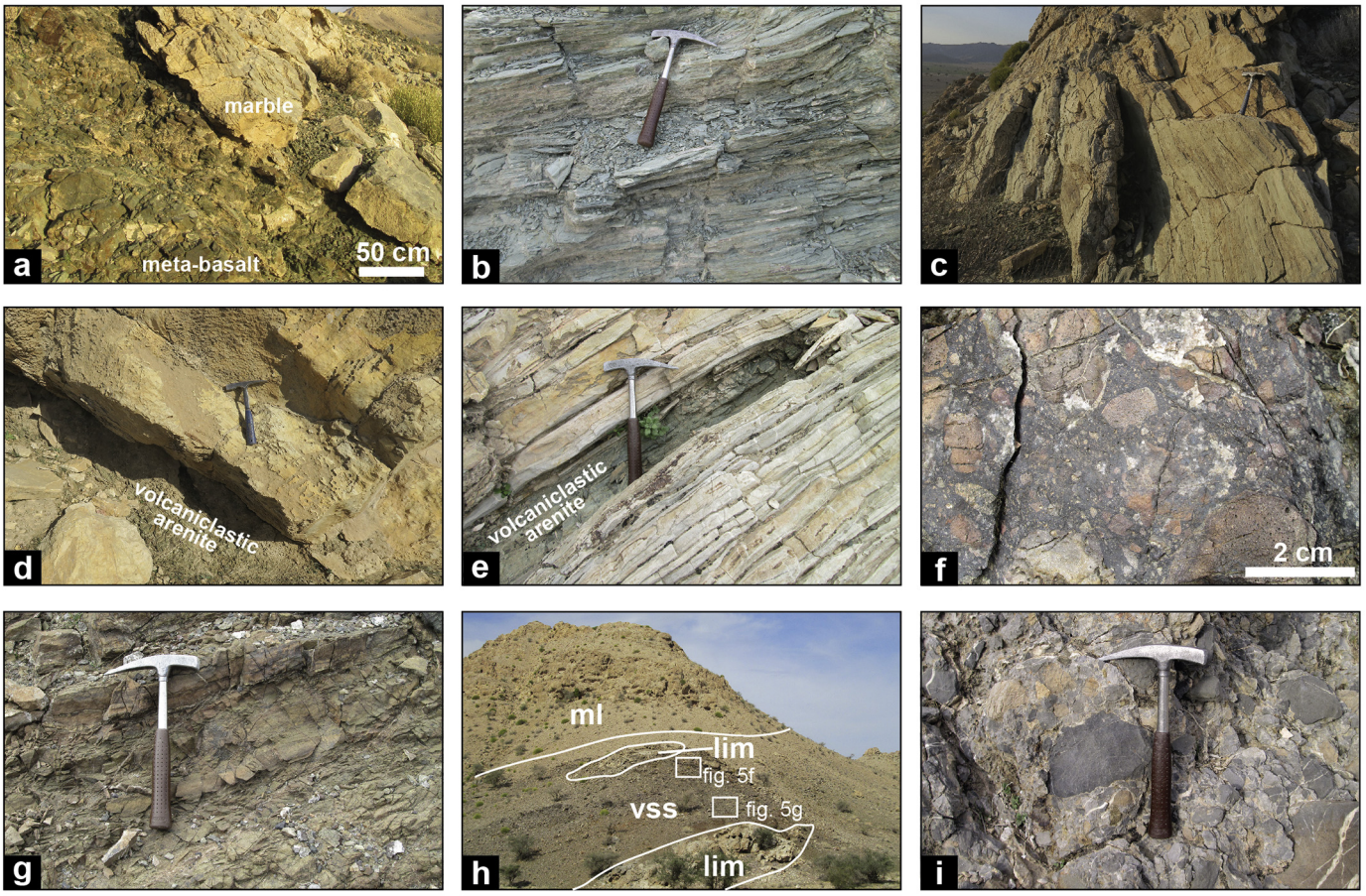

Fig. 5. Field occurrence of the Durkan Complex in the Zandan transect: (a) stratigraphic relationships between the Meta-Volcanic Sequence and the Massive Marble; (b) foliated meta-volcaniclastic arenites; (c) massive marble; (d) intercalation of greenish meta-volcaniclastic arenites within the marble; (e) medium- to thin-bedded meta-limestone alternated with shale and meta-volcaniclastic arenites; (f) volcanic breccia with clast of vesicular basaltic rocks set in fine-grained volcanic matrix; (g) greenish volcaniclastic arenites; (h) panoramic view of the contact between the Volcano-Sedimentary Sequence (VSS) and the Massive Limestone (ml) lithostratigraphic units. Intercalation of massive limestone (lim) occur in the VSS. The locations of Fig. 5f and 5g are also indicated; (i) clast-supported carbonatic breccias.

3.2.2. The Manujan transect

This transect is located to the south of the town of Manujan (Fig. 2). In this area, the NNE-directed strike-slip Sabzevaran Fault truncates the low angle tectonic contact between the Durkan and Bajgan Complexes with dextral displacement (Figs. 2 and 3b). This fault also shows a dip-slip displacement, causing the uplifting of the eastern fault block (Figs. 2 and 3b). In this transect, the Durkan Complex occur, within a reverse fault zone, as lenticular and along strike discontinuous tectonic slices, which are several tens of meters thick (Figs. 3b and 6a). This fault zone juxtaposes the Durkan Complex onto the Bajgan Complex with the interposition of a tectonic slice of *Nummulites*-bearing siliciclastic rocks (Fig. 6b) of the Eocene succession (Figs. 3b and 6a). This evidence suggests a post-Eocene age for this reverse fault zone, which is, in turn, crosscut by the dextral Sabzevaran Fault (Figs. 2 and 3b).

In the Manujan transect, the Durkan Complex consists of non-metamorphic succession, which defines the Cherty-Limestone and Basalt lithostratigraphic unit of Fig. 3b3. The sequence consists of a complex pelagic succession (Fig. 6c) composed by the alternation of pinkish to whitish cherty-limestones (Fig. 6d), thin- to medium-bedded silicified limestones (Fig. 6e), subordinate thin-bedded red cherts (Fig. 6f), reddish siliceous shales and marls. In addition, two levels of pillow lava basalts are intercalated in the pelagic sequence (Fig. 3b3). The basaltic lava flows show clear primary stratigraphic relationships with sedimentary rocks and lateral sudden change in thickness, up to the pinch-out of the volcanic level into the pelagic succession (Fig. 6g). The primary relationships among the pillow lava flows and the pelagic sequence are also indicated by soft clasts of the pelagic carbonate sequence inside the pillow lavas (Fig. 6h).

3.2.3. The Chah Shahi 1 transect

This transect is located just to the east of the village of Chah Shahi. It consists of three tectonic slices (Figs. 2 and 3c). Two of the slices show similar stratigraphic successions and are tectonically juxtaposed by a NE-dipping thrust (Fig. 3c1, c2). The third succession crops out in the SSW sector showing stratigraphic features (see Fig. 3c3) that are quite different from those of the other two.

The westernmost and structurally lowermost unit (Fig. 3c3) includes a non-metamorphic succession, which consists of several levels of pillow lava flows associated with radiolarian cherts and volcaniclastic arenites (Fig. 7a), interlayered with red cherty-limestones, reddish shales and minor shaly-marls. This stratigraphic succession shows significant analogies with the Cherty-Limestone and Basalt lithostratigraphic unit of the Manujan transect (see Section 4.2 and Fig. 3b3).

In contrast, the stratigraphic successions preserved in the other two slices of the Chah Shahi 1 transect are characterized by a Volcanic Sequence that stratigraphically passes to a Volcano-Sedimentary Sequence. The latter is, in turn, followed by a mainly carbonatic sedimentary succession (Fig. 7b), which only consists of one lithostratigraphic unit, hereafter named as Limestone and Shale (Fig. 3c1, c2). The Volcanic Sequence shows massive volcanic rocks (Fig. 7c) alternated with less abundant coarse-grained volcaniclastic

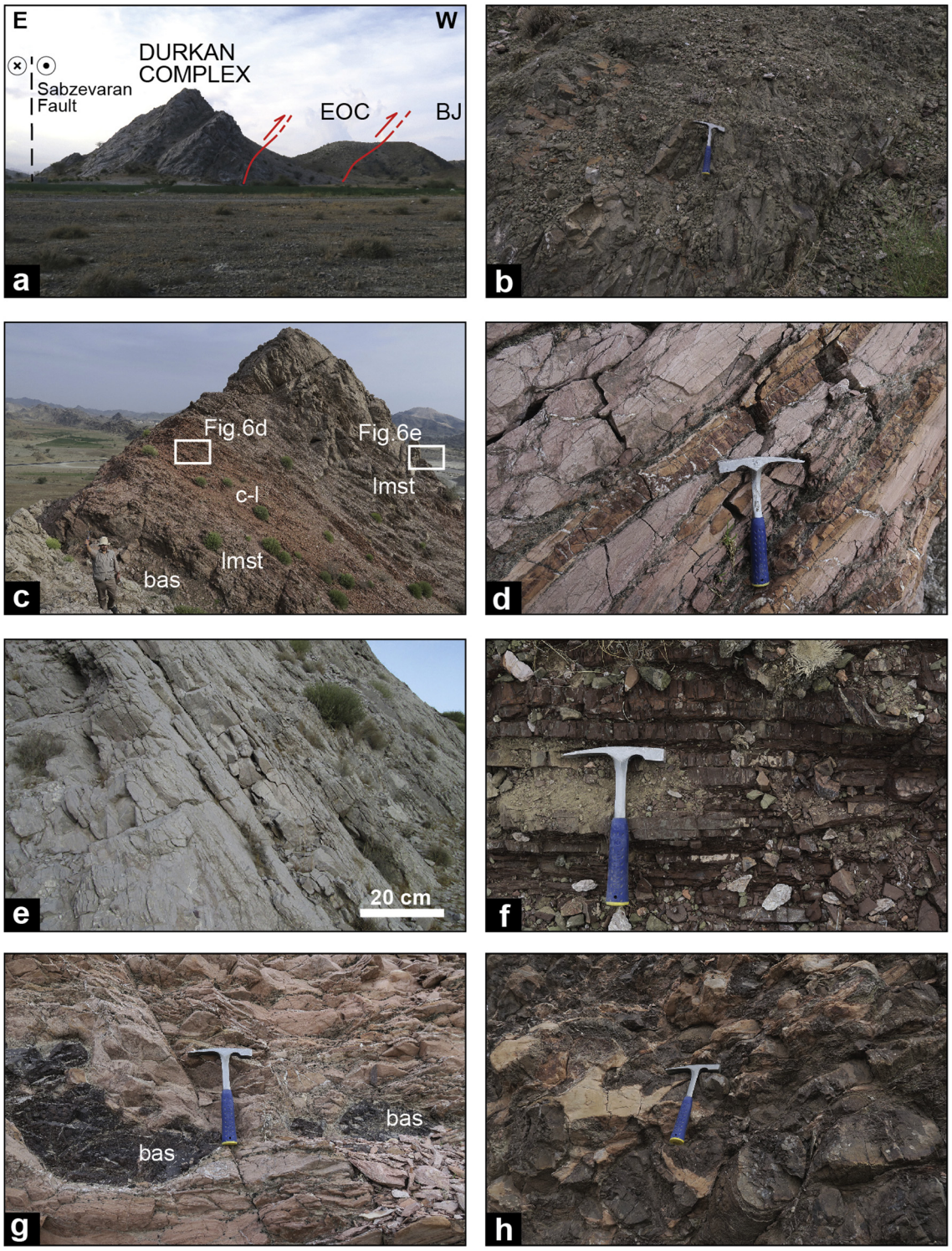

Fig. 6. Field occurrence of the Durkan Complex in the Manujan transect: (a) panoramic view of the reverse fault zone between the Bajgan Complex (BJ) and the Durkan Complex in the Manujan transect. A tectonic slice of Eocene siliciclastic succession (EOC) is interposed between the two Complexes. The location of the buried right-later Sabzevaran Fault is also shown; (b) detail of greenish arenites within the Eocene succession tectonically juxtaposed to the Durkan Complex (hammer for scale); (c) panoramic view of the pelagic sequence of the Cherty-Limestone and Basalt lithostratigraphic unit (bas: pillow basalt; lmst: limestone; c-l: cherty-limestone). The position of field occurrences shown in Fig. 6d, and e are also shown; (d) alternating beds of pinkish cherty-limestone; (e) whitish limestones from the Cherty-Limestone and Basalt; (f) alternating chert and shale; (g) detail of the pinch out of the pillow basalt flows (bas) within the pelagic sequence, suggesting primary stratigraphic relationships between lavas and pelagic sedimentary rocks; (h) soft clasts of marly-limestone within pillow lava flows.

arenites. The Volcano-Sedimentary Sequence is characterized by alternating volcaniclastic arenites (Fig. 7d) and varicoloured (greenish and purplish – to reddish) shales and siltstones (Fig. 7b, e). Compared to the Volcanic Sequence, this sequence is characterized by the subordinate abundance of massive volcanic rocks, as well as by the exclusive occurrence of purplish and greyish limestones, whose abundance increase

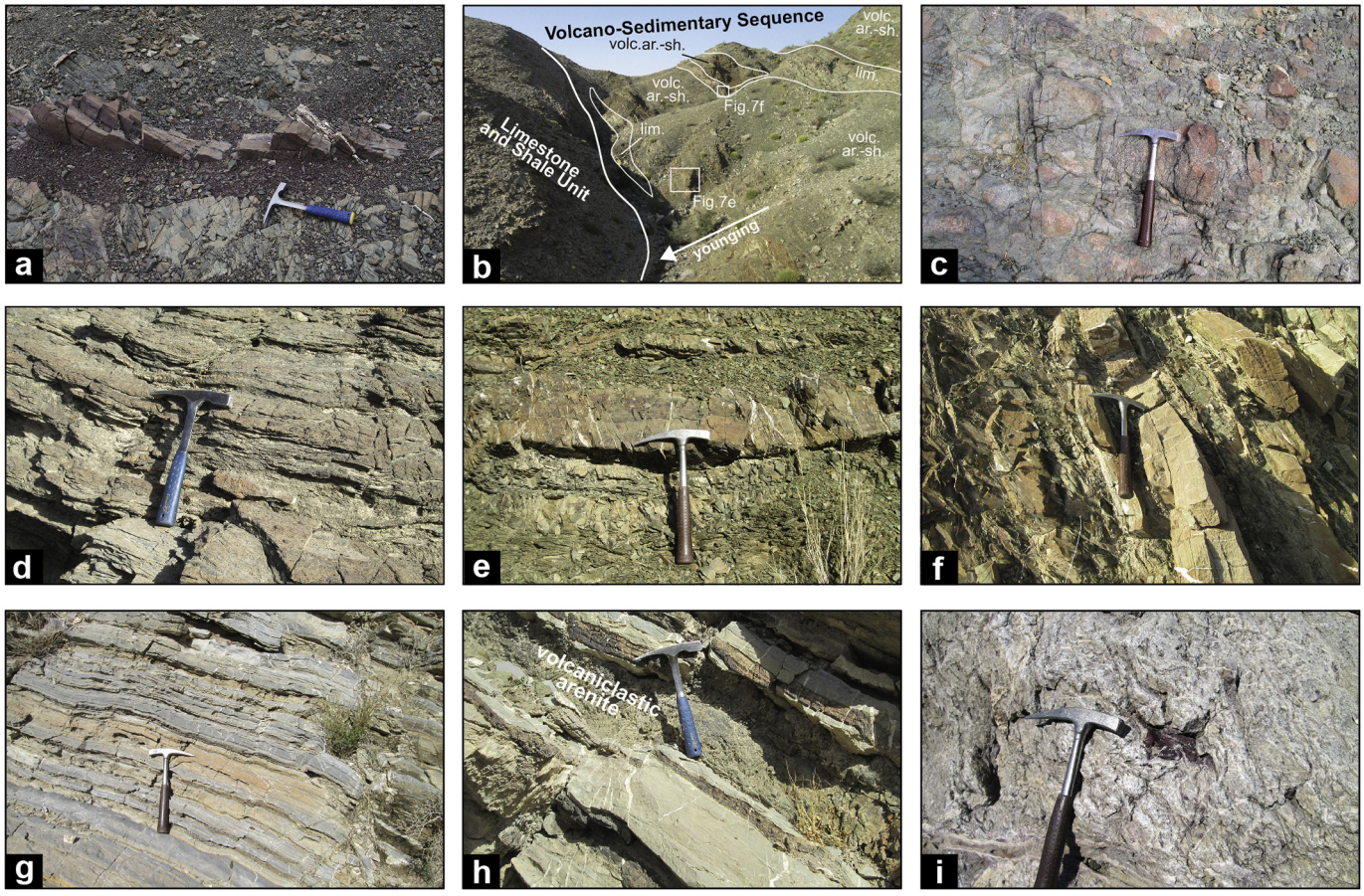

Fig. 7. Field occurrence of the Durkan Complex in the Chah Shahi 1 transect: (a) thin chert beds alternated with pillow basalt (hammer for scale); (b) panoramic view of the stratigraphic transition from the Volcano-Sedimentary Sequence and the Limestone and Shale along an overturned fold limb; abbreviations: volc. ar.-sh.: volcaniclastic arenite and shale; lim.: limestone. The position of Fig. 7e and f are indicated; (c) volcanic rocks in the Volcanic Sequence; (d) alternating volcaniclastic arenites and shales (Volcano-Sedimentary Sequence); (e) volcaniclastic arenites alternating with greenish shale from the Meta Volcano-Sedimentary Sequence; (f) greyish limestone alternating with greenish shale from the upper part of the Meta Volcano-Sedimentary Sequence; (g) thin bedded limestones alternating with shaly-marls (Limestone and Shale); (h) detail of greenish volcaniclastic arenites interbedded with cherty-limestone in the Limestone and Shale; (i) clast-supported carbonatic breccia in the Limestone and Shale.

toward the top of the succession (Figs. 3c1, c2 and 7b, f). The succession of the Limestone and Shale lithostratigraphic unit consists of greyish to light blue turbiditic limestones alternating with shaly-marls and shales, as well as less abundant cherty-limestones and volcanoclastic arenites (Figs. 3c1, c2 and 7g, h). Locally, lenticular thick beds of whitish massive limestones and carbonatic breccia occur at the base of the succession (Fig. 3c2). The breccia shows clast-supported texture and its composition is largely characterized by white limestone clasts set in a fine-grained carbonatic matrix (Fig. 7i).

3.2.4. The Chah Shahi 2 transect

This transect is located few kilometres to the north of the village of Chah Shahi (Fig. 2). It is characterized by an uppermost tectonic slice showing a coherent stratigraphic succession bounded at the base by an NNW-striking thrust zone (Figs. 3d and 8a). This thrust zone displays a complex internal structure and juxtaposes the Durkan Complex to the Bajgan Complex (Fig. 3d). It displays interlacing faults segments that bound a series of lenticular slices of hundreds of metres in length (Fig. 8a). These tectonic slices show successions that differ in either lithostratigraphy or metamorphism. In the following discussion, we will summarize the complex field evidence by giving a schematic description of the main types of successions cropping out in this fault zone. For the sake of simplicity, we will describe first the successions tectonically deformed within the fault zone and then the coherent stratigraphic succession.

The structurally lowermost tectonic slice that is observable in the thrust zone is represented by a Meta Volcano-Sedimentary Sequence showing subgreenschist facies metamorphism. It consists of alternating marbles and shales with minor abundant massive meta-volcanic rocks and meta-volcaniclastic arenites (Fig. 3d1). This slice is overlain by a tectonic slice showing a non-metamorphic stratigraphic succession, which includes a Volcanic Sequence passing upward to a Volcano-Sedimentary Sequence (Fig. 3d2). A significant feature of this succession is the abundant occurrence of massive volcaniclastic breccias (Figs. 3d2 and 8b). These breccias are characterized by fragments of aphyric, vesicular basalts, porphyritic basalts, mafic holocrystalline rocks (i.e., microgabbros and dolerites) as well as plurimillimetric pyroxene crystals (Fig. 8c). These fragments are set in a matrix exclusively made up of fine-grained volcanic material represented by crystals and altered volcanic glass (Fig. 8c). The fault zone is characterized in the uppermost part by two distinct slices showing pervasive metamorphic recrystallization under subgreenschist facies conditions (Fig. 3d3, d4). The lower slice is characterized by coarse-grained and sheared meta-volcaniclastic arenites alternated with meta-limestones and shales (Fig. 3d3). This succession shows many similarities with the succession of the Volcano-Sedimentary Sequence cropping out in other transects (e.g., Fig. 3c1, c2), as well as in other tectonic slices of this transect (e.g., Fig. 3d1). The meta-volcaniclastic rocks show a foliation defined by a fine-grained aggregate of chlorite, oxide, calcite and minor albite and quartz. The uppermost tectonic slice of the fault zone consists of a

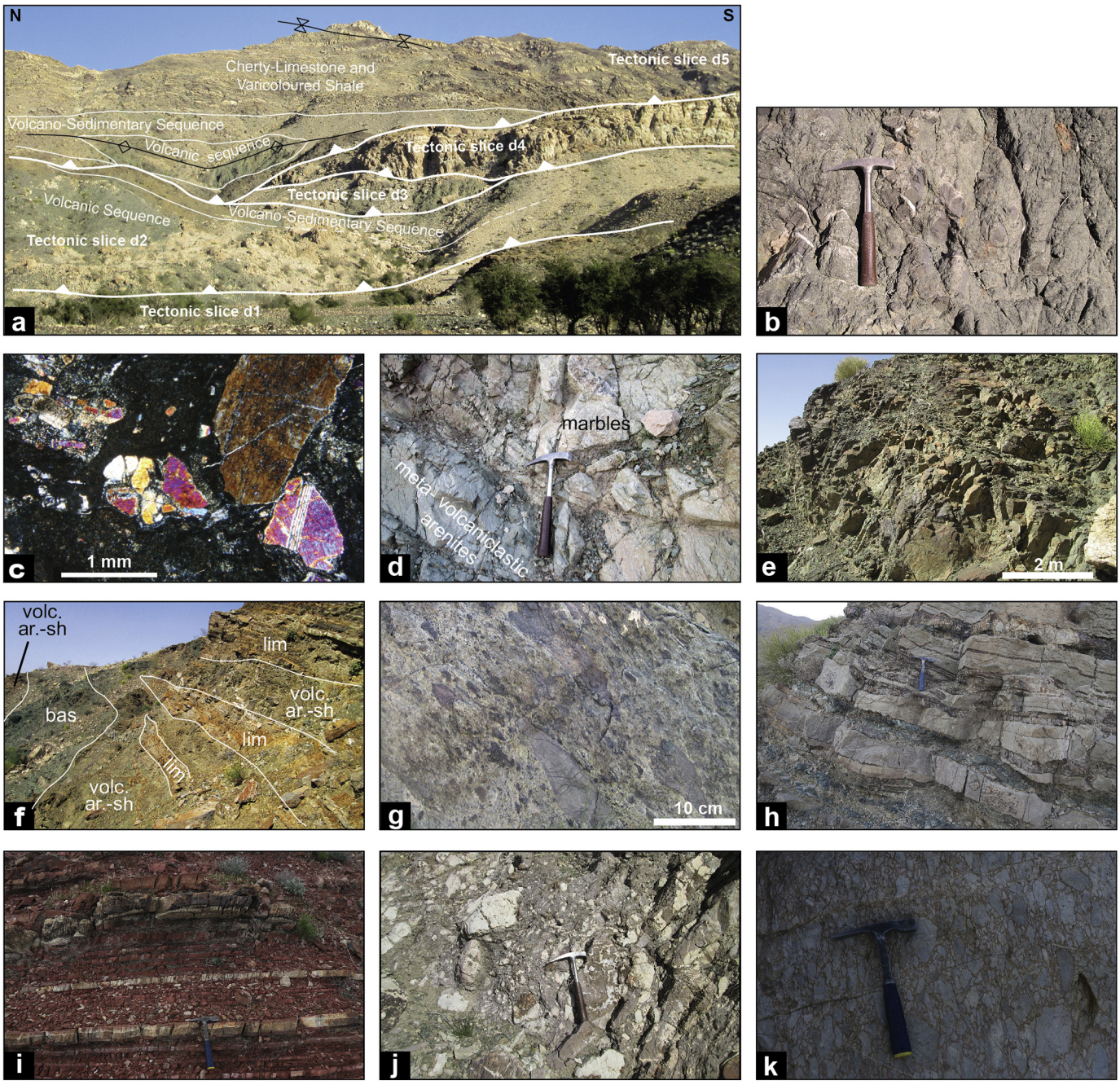

Fig. 8. (a) Panoramic view of the Chah Shahi 2 transect showing the thrust zone (tectonic slices e1 to e4) and the overlying coherent succession (tectonic slice e5). In the latter are also indicate the axial plane of macro-scale antiformal and sinformal folds; Field occurrence and photomicrographs of the Durkan Complex in the Chah Shahi 2 transect (b–d: thrust zone; e–k coherent succession): (b) volcaniclastic breccia showing clast of different types of volcanic rocks set within a greenish arenitic matrix (hammer for scale); (c) photomicrograph of clast-supported volcaniclastic breccia, characterized by pyroxene crystals and volcanic fragments with different textures (aphyric, porphyritic and holocrystalline rocks) set in a fine-grained matrix made up of volcanic material (glass and microlite); (d) massive marble showing stratigraphic relationships with meta-volcaniclastic arenite; (e) massive volcanic rocks alternated with volcaniclastic arenites from the Volcanic Sequence; (f) panoramic view of the Volcano-Sedimentary Sequence showing primary stratigraphic alternation of massive basaltic lava (bas), volcaniclastic arenites and greenish shale (volc. Are.-sh.), and limestone and shale (lim.); (g) matrix-supported breccia from the Volcano-Sedimentary Sequence showing limestone and shale clasts in a fine-grained greyish to greenish matrix; (h) alternating cherty-limestone and varicoloured shale from the Cherty-Limestone and Varicoloured Shale; (i) reddish cherts and shale alternated with brownish cherty-limestone; (j) matrix-supported breccia showing decametric blocks enclosed within pinkish to greyish fine-grained carbonatic matrix; (k) detail of the clast-supported breccias showing eterometric and angular clasts of carbonatic rocks set within a fine-grained matrix.

sequence of massive marble locally alternated with greenish meta-volcaniclastic arenites (Figs. 3d4 and 8d). The same succession is also observed in some other tectonic slices within the fault zone and shows significant analogies with the Massive Marble lithostratigraphic unit cropping out in the Zandan transect (see Fig. 3a1).

The coherent succession consists of three lithostratigraphic units (Fig. 3d5). From the lower to the upper stratigraphic position, these units are: (i) the Volcanic Sequence; (ii) the Volcano-Sedimentary Sequence; (iii) the Cherty-Limestone and Varicoloured Shale. The basal Volcanic Sequence includes massive volcanic rocks alternated with coarse-grained volcaniclastic breccias and arenites (Fig. 8e). The volcaniclastic breccia is characterized by clasts of aphyric, porphyritic and vesicular volcanic rocks, as well as either fractured or euhedral pyroxene crystals, up to 1–2 cm in size. These materials are set in a

heterogeneous fine-grained and foliated matrix, mainly consisting of chlorite aggregate, clay mineral and less abundant calcite. The Volcanic sequence shows a stratigraphic and transitional passage to the Volcano-Sedimentary Sequence (Fig. 8f). The latter consists of greenish volcaniclastic arenites interbedded with varicoloured (purplish and reddish - to greenish) shales and siltstones, as well as purplish to pinkish and light grey limestones (Figs. 3d5 and 8f). In addition, thick lenticular beds of volcaniclastic breccias and polygenic breccias are interbedded in the sequence (Fig. 3d5). The volcaniclastic breccias observed in the Volcano-Sedimentary Sequence is texturally and compositionally comparable to that observed in the underlying Volcanic Sequence. In contrast, the polygenetic breccias display matrix-supported texture with clasts up to 10–15 cm (Fig. 8g). The clasts include both volcanic and sedimentary rocks fragments (i.e., aphyric and vesicular basalts, grey limestone, reddish to purplish shale), and are embedded within a foliated, mainly carbonatic, fine-grained matrix. The succession continues upward with the Cherty-Limestone and Varicoloured Shale lithostratigraphic unit (Fig. 3d5). This unit is characterized by thin to medium thick beds of limestone, cherty limestone, and calcareous turbidites alternating with varicoloured shales (Figs. 3d5 and 8h), reddish cherts and minor cherty-limestones (Fig. 8i), as well as minor volcaniclastic turbidites. Rare basaltic rocks intrude the successions, forming tabular sills. In addition, thick beds of breccias are interbedded within the successions of this lithostratigraphic unit at different stratigraphic position (Figs. 3d5 and 8j). The breccias show both clast- and matrix-supported textures and are characterized by centimetric to decimetric limestone clasts and subordinate clasts of volcanic rocks. The clasts are angular to sub-angular in shape and are enclosed within a fine-grained and pinkish to reddish carbonatic matrix (Fig. 8j, k).

4. Biostratigraphy

Biostratigraphy is based on data from foraminifera, radiolarians and calcareous nannofossils analyses that were performed on a total of 37 samples taken from the studied transects. The aim of the biostratigraphic studies was to date the sedimentary rocks associated with the volcanic rocks, in order to provide age constraints for the magmatic activity. Due to the intense deformation that affected the successions of the Durkan Complex and resulted in a poor preservation of fossils, an integration of different biostratigraphic methods was necessary for obtaining robust age data, as well as for correlating the different successions. Calcareous nannofossils, foraminifera, and radiolaria were analysed on samples from Manujan and Chah Shahi 1 transects, whereas the Zandan transect has been investigated only by foraminifera. The detailed list of samples is given in Supplementary Table 1.

4.1. Foraminifera

Foraminifera were analysed in thin sections. Unfortunately, the state of preservation is generally poor and foraminiferal tests are often recrystallized and/or deformed thus hampering in several cases a correct identification. The main results are reported below.

From the Zandan transect only samples MK901–904, and MK906 provided age information. Specifically, samples from MK901 to MK904 are from the Massive Limestone lithostratigraphic unit and they are grainstones-packstones with ooids and pisoids (MK904) containing shallow-water assemblages that include: *Corallinales*, benthic foraminifera such as common *Quinqueloculina* associated with textularids, *Pseudolituonella, Chrysalidina*, *Nezzazata* and *Pseudorhapydionina*. The last genus is stratigraphically restricted and indicates a late Cenomanian age (Fig. 10) (Loeblich and Tappan, 1988; Afghah et al., 2014). Fossils from sample MK905 are very badly preserved to be recognizable with the exception of rare alveolinids. Sample MK906 that comes from a turbiditic level belonging to the Volcano-Sedimentary Sequence, includes slabs of mudstones showing deep recrystallization (dolomites?). Some of these slabs contain rare “ghost” of plantkic foraminifera. The occurrence of one planktic foraminifer bearing double-keeled chambers suggests a Late Cretaceous age.

Samples MK822 and MK886 are grainstones with benthic foraminifera (miliolids, textularids) and red algae but age diagnostic taxa are lacking whereas the arenites MK887, MK888, MK893, MK897, MK897b do not display recognizable taxa.

The samples MK468 and MK472 from the siliciclastic successions in the Manujan transect are arenites preserving very rare alveoloinids and *Nummulites* of Eocene age. Sample MK362 is from the Cherty-Limestone and Basalt lithostratigraphic unit and it consists of a wackestone rich in planktic foraminifera that include *Globotruncanita stuarti, G. startiformis, Globotruncana arca, G. bulloides, G. falsostuarti, G. orientalis, Contusotruncana fornicata, C. plummeare, Rugoglobigerina rugosa, Ventiabrella* sp. and *Radotruncana calcarata*. The occurrence of the last species allows us to refer the sample to the total range Zone *R. calcarata* (Coccioni and Premoli Silva, 2015) of upper Campanian age (Fig. 10).

Only the samples MK854 and MK849 from the Volcano-Sedimentary Sequence in the Chah Shahi 1 transect provided age information. Specifically, the occurrence of rare specimens of *Rotalipora cushmani*, though poorly preserved, refers these samples to the Zone *R. cushmani* (Coccioni and Premoli Silva, 2015) of upper Cenomanian age (Fig. 10). These samples preserve several traces of organic carbon. Preservation of organic carbon is frequent in levels close to the sedimentary expression of the Oceanic Anoxic Event 2 that is recorded in the latest Cenomanian (Schlanger and Jenkyns, 1976). Samples MK847, MK852 and MK853 from the Limestone and Shale succession contain radiolarians but no recognizable planktic foraminifera. However, the microfacies of these samples that include numerous traces of organic carbon are similar to those from the previous samples containing *R. cushmani*. It is therefore possible to indicate a latest Cenomanian age also for the MK847, MK852 and MK853 samples.

4.2. Calcareous nannofossils

For the study of calcareous nannofossils, samples were prepared following standard preparation techniques for light microscopy observation (simple smear slide, as described in Bown and Young, 1998). Observation were performed through a Leitz-Laborlux12 POL microscopy with cross polarized light at 1250 magnification. Data were collected with the semi-quantitative counting method suggested by Backman and Shackleton (1983). In this study, specimens referable to the recognized taxa were counted on 200 fields of view and then were expressed relative to a unit area (number of specimens for mm^2). Data are summarized in Supplementary Table 2, whereas microphotos of selected calcareous nannofossil taxa are shown in Fig. 9.

Calcareous nannofossils analyses were performed on 8 samples collected from the Cherty-Limestone and Basalt unit (Manujan transect), the Limestone and Shale (Chah Shahi 1 transect). Unfortunately, most of these samples were found to be barren and/or contain assemblages impossible to be recognized due to the high degree of diagenetic and/or metamorphic recrystallization. The samples from the marls of the Cherty-Limestone and Basalts lithostratigraphic unit (Manujan transect) contain assemblages very scarce and poorly preserved, but it was possible to recognize some useful taxa. On the contrary the samples from the Limestone and Shale unit in the Chah Shahi 1 transect were found to be barren. Assemblages present very low diversity; the only genera recognized were *Micula, Broinsonia, Cyclagelosphaera, Eprolithus, Thoracosphaera* and *Watznaueria*. More difficult was the identification of species because of diagenetic process that affected these calcareous fossils (heavily etched and overgrown). However, the common occurrence of *Micula* and the occurrence, even if rare, of *Broinsonia* belonging to the *parca* group, allow us to relate the Cherty-Limestone and Basalt lithostratigraphic unit to the Coniacian-Campanian time span (Fig. 10).

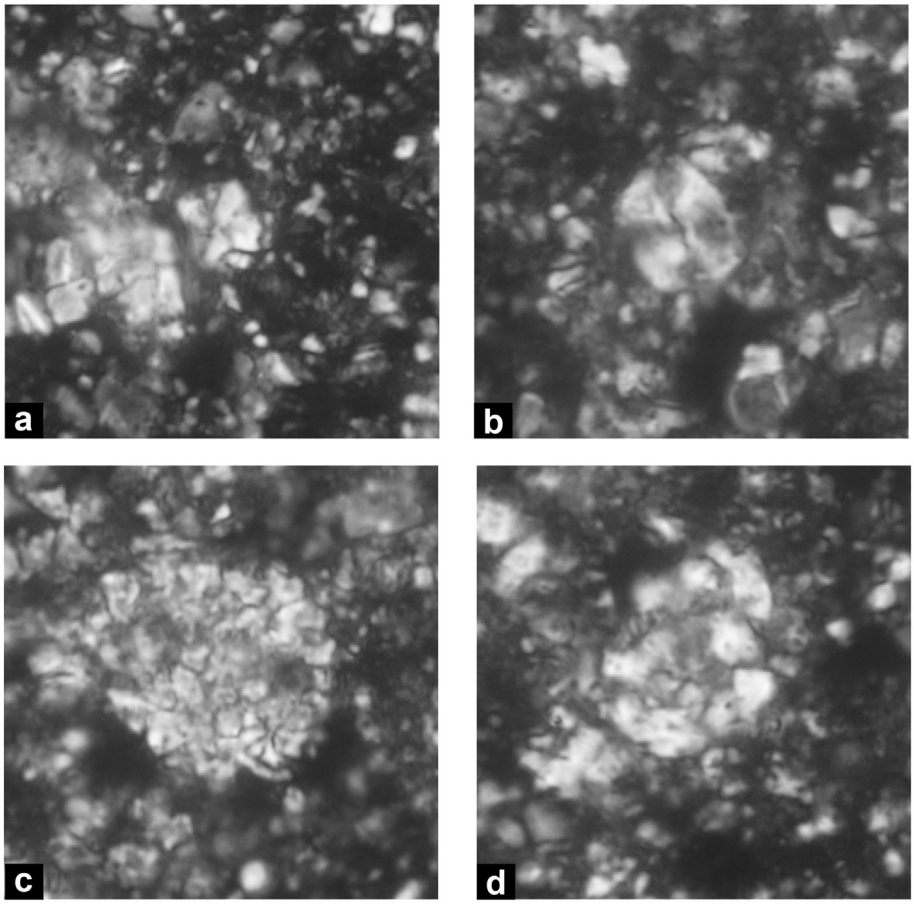

Fig. 9. Microphotographs of selected calcareous nannofossil taxa. Light Microscope photographs are in Cross Polarized Light. (a) *Micula*. Sample MK464. (b) *Watznaueria* cf. *barnesiae*. Sample MK464. (c) *Thoracosphaera*. Sample MK464. (d) *Broinsonia* cf. *parca*. Sample MK464.

4.3. Radiolarian

The sampled radiolarites were etched by a first treatment with hydrochloric acid at 3.7% for removing the carbonates present in some samples and for avoiding the formation of fluorite in the residues. The successive treatments, with hydrofluoric acid at 2%, permitted to extract radiolarians from the samples. References for the treatment used are given in supplementary text.

The residues of the different treatments were preliminarily observed by means of a reflected light stereomicroscope then, the best-preserved radiolarians specimens were studied using a scanning electron microscope (SEM). The examined samples yielded radiolarians with very poor to moderate preservation and the principal radiolarian markers are shown in Fig. 11. References used for determining the first and last occurrence of the radiolarian taxa are given in the Supplementary text.

Radiolarian determinations were performed on 8 samples collected from the Cherty-Limestone and Basalt lithostratigraphic unit in both the Manujan and Chah Shahi 1 transects. In detail, samples MK363, MK367, MK466, MK469, and MK471 were collected in the Manujan transect whereas samples MK 374, MK378, and MK796 were sampled in the Chah Shahi 1 transect. Unfortunately, samples MK363, MK466, MKMK374, and MK378 were found to be barren or display very poor preservation of radiolarians hampering any age assignments. In the following text we reported the results of radiolarian determinations only for the samples meaningful for the age determinations.

4.3.1. Manujan transect

Sample MK367 yielded radiolarians with moderate preservation and the following taxa were determined: *Alievium* sp. cf. *A. murphyi* Pessagno, *Alievium* sp., *Archaeocenosphaera* (?) sp., *Archaeodictyomitra* sp. cf. *A. montisserei* (Squinabol), *Archaeodictyomitra* sp., *Becus* (?) sp., *Cryptamphorella macropora* Dumitrica, *Cryptamphoraella sphaerica* (White), *Cryptamphoraella* (?) sp., *Crucella* sp. cf. *C. messinae* Pessagno, *Dictyomitra formosa* (Squinabol), *Dictyomitra* sp. cf. *D. formosa* (Squinabol), *Dictyoprora sallilum* (Foreman), *Dictyoprora urna* (Foreman), *Dictyoprora* sp. aff. *D. urna* (Foreman), *Dictyoprora* sp. cf. *D. urna* (Foreman), *Foremanina* (?) sp., *Parvimitrella* sp. cf. *P. mediocris* (Tan) sensu O'Dogherty (1994), *Parvimitrella* sp. cf. *S. japonica* (Nakaseko & Nishimura), *Praeconocaryomma* (?) sp., *Pseudoaulophacus pargueraensis* Pessagno, *Pseudoaulophacus* sp. cf. *P. lenticulatus* (White), *Pseudoaulophacus* sp. cf. *P. putahensis* Pessagno, *Pseudoaulophacus* sp., *Rhopalosyringium* sp. The occurrence of *Dictyoprora sallilum* (Foreman) with *Dictyoprora urna* (Foreman) indicate early Coniacian-late Campanian age of the sample MK367 (Fig. 10).

Range Dictyoprora sallilum (Foreman). Early Coniacian, *Theocampe urna* Zone of Riedel and Sanfilippo (1974) (*Theocampe urna* Zone: early Coniacian-late Santonian in Sanfilippo and Riedel, 1985) to late Maastrichtian, *Amphipyndax tylotus* zone of Foreman (1977) (*Amphipyndax tylotus* Zone late Campanian-late Maastrichtian in Sanfilippo and Riedel, 1985).

Range Dictyoprora urna (Foreman). Early Coniacian, *Theocampe urna* Zone of Riedel and Sanfilippo (1974) (*Theocampe urna* Zone: early Coniacian–late Santonian in Sanfilippo and Riedel, 1985) to late Campanian, *Amphipyndax pseudoconulus* Zone after Riedel and Sanfilippo (1974) emended in Foreman (1977) (*Amphipyndax pseudoconulus* Zone: Campanian in Sanfilippo and Riedel, 1985).

The sample MK469 contained radiolarian in poor/moderate preservation and the following taxa were recognized: *Archaeodictyomitra* sp.

cf. *A regina* Campbell & Clark, *Dictyoprora urna* (Foreman), *Dictyomitra* sp. cf. *D. multicostata* Zittel, *Dictyomitra* sp. cf. *D. formosa* (Squinabol), *Dictyomitra* sp., *Parvimitrella* sp. It is possible to indicate an early Coniacian-late Campanian age for the sample MK469 due to the presence of *Dictyoprora urna* (Foreman) (range: *Theocampe urna - Amphipyndax pseudoconulus* Zones) (Fig. 10).

The sample MK471 contained radiolarians with poor preservation and the assemblage of this sample includes: *Alievium* (?) sp., *Archaeocenosphaera* sp., *Dictyoprora urna* (Foreman), *Praeconocaryomma* (?) sp. The age of the sample MK471 is early Coniacian–late Campanian (Fig. 10) for the presence of *Dictyoprora urna* (Foreman) (range: *Theocampe urna - Amphipyndax pseudoconulus* Zones).

4.3.2. Chah Shahi 1 transect

Sample MK796 contains radiolarians with poor/moderate preservation, and the assemblage includes the following taxa: *Alievium* sp., *Archaeodictyomita* sp., *Crucella* sp., *Dictyoprora urna* (Foreman), *Praeconocaryomma* (?) sp., *Pseudoaulophacus* sp. cf. *P. lenticulatus* (White), *Alievium* sp. The presence of *Dictyoprora urna* (Foreman) suggests an early Coniacian-late Campanian age (range *D. urna: Theocampe urna-Amphipyndax pseudoconulus* Zones) for this samples (Fig. 10).

To summarize, the results of the radiolarians biostratigraphic study indicates early Coniacian–late Campanian age for the Cherty-Limestone and Basalt lithostratigraphic unit in both the Manujan and Chah Shahi 1 transects (Fig. 10).

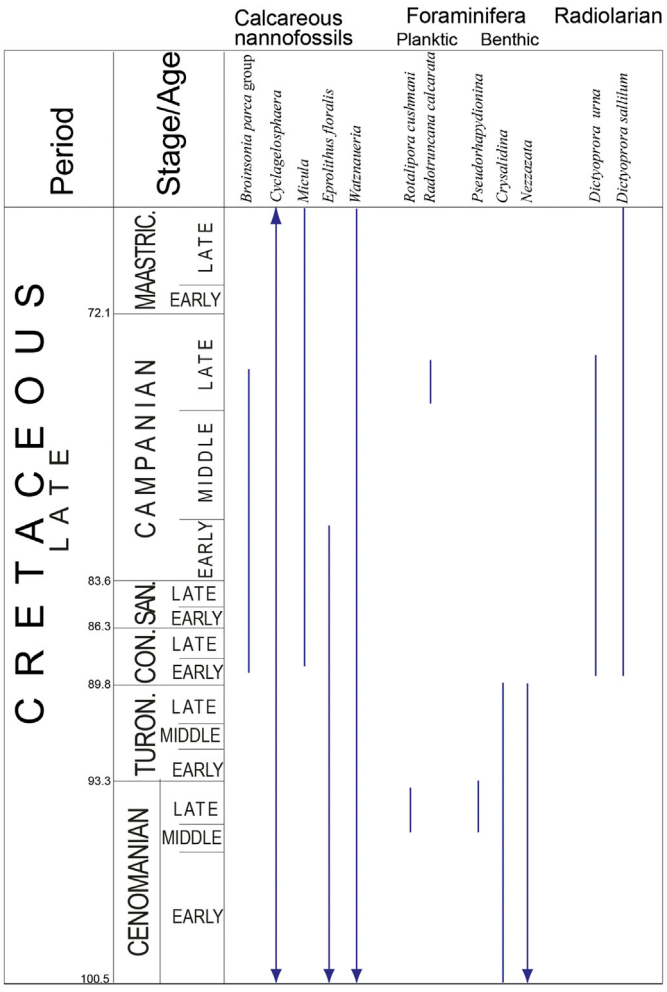

Fig. 10. Range chart showing the distribution of calcareous nannofossil taxa, foraminifera taxa and radiolarian taxa recognized in the stratigraphic successions of the Durkan Complex. Chronostratigraphy and age of the stage boundaries after Gradstein et al. (2012).

5. Petrography and geochemistry of the volcanic rocks

Eleven samples of volcanic rocks were selected for petrographic and geochemical investigations. These samples have been collected in different lithostratigraphic units of all the studied transect (see Table 1 and Fig. 3b–e for their location with respect to the different transects and units). Petrography and geochemistry of these rocks are used here to assess nature, chemical affinity and tectono-magmatic setting of formation of the volcanic rocks cropping out in the different units of the Durkan Complex, as well as their possible environment of eruption. A detailed petrological study aimed to establish the petrogenetic mechanism (i.e., mantle source composition, partial melting processes, shallow-level magmatic evolution, etc.) is beyond the scope of this paper and it will be the object of further investigations.

5.1. Petrography

The studied volcanic rocks are represented by basalts. Most of them are affected by variable degrees of alteration, which resulted in different extent of replacement of the primary magmatic minerals with secondary phases. Nonetheless, their original magmatic textures are still recognizable, and they will be used in the following petrographic descriptions. Fresh plagioclase is very rare, and it is usually pseudomorphosed by fine grained assemblage of albite, calcite and sericite. Similarly, olivine crystals, even though extremely rare, are commonly replaced by iddingsite and serpentine + Fe-Ti oxides. Though fresh clinopyroxene crystals are present both as phenocrysts and groundmass minerals, clinopyroxene alteration commonly occurs as pseudomorphic replacement by chlorite or actinolitic amphibole. When present, the volcanic glass has been replaced by an assemblage of chlorite and clay minerals.

Basalts from the Durkan Complex show a great variety of textures. They include basalts showing aphyric (PI <10) and porphyritic (PI = 15–60) texture, as well as rocks displaying coarser-grained doleritic texture. The phenocrysts mainly consist of laths of plagioclase and clinopyroxene, showing euhedral to subhedral shape. Fe-Ti oxides are abundant in the porphyritic variety. In addition, rare olivine phenocrysts occur in a few samples. Both aphyric and porphyritic varieties are characterized by hypocrystalline groundmass showing different types of textures. In particular, in the aphyric rocks the groundmass is characterized by intersertal to microcrystalline texture, whereas intergranular to microcrystalline texture are the prevalent groundmass texture in the porphyritic variety. Basalts with coarse-grained doleritic texture show holocrystalline inequigranular texture, defined by euhedral to subhedral plagioclase and clinopyroxene crystal, plurimillimetric in size. These crystals are surrounded by a fine-grained crystalline aggregate made up of plagioclase, clinopyroxene, Fe-Ti oxides, as well as rare quartz. Some of the aphyric and porphyritic basalts from Durkan Complex show amygdaloidal texture. They are characterized by rounded to sub-rounded vesicles filled by calcite, chlorite, and chalcedony. As a peculiar feature, the amount (volume %) of vesicles show a great range of variation. The significance of this feature will be discussed in detail in Section 5.3.

5.2. Geochemistry

Whole rock major and trace elements composition of the selected basaltic samples was determined by X-ray fluorescence spectrometry at the Ferrara University. The results are presented Table 1. Analytical methods, as well as accuracy and detection limits are reported in Supplementary Table 3. Petrographic analyses indicate that most of the basalts from the Durkan Complex have undergone secondary alteration (e.g., sub-marine hydrothermal alteration, polyphase deformation, subgreenschist facies metamorphism). Secondary alteration commonly implies remobilization of large ion lithophile elements (LILE) and many major elements. In contrast, many incompatible elements (e.g., Ti, P, Zr,

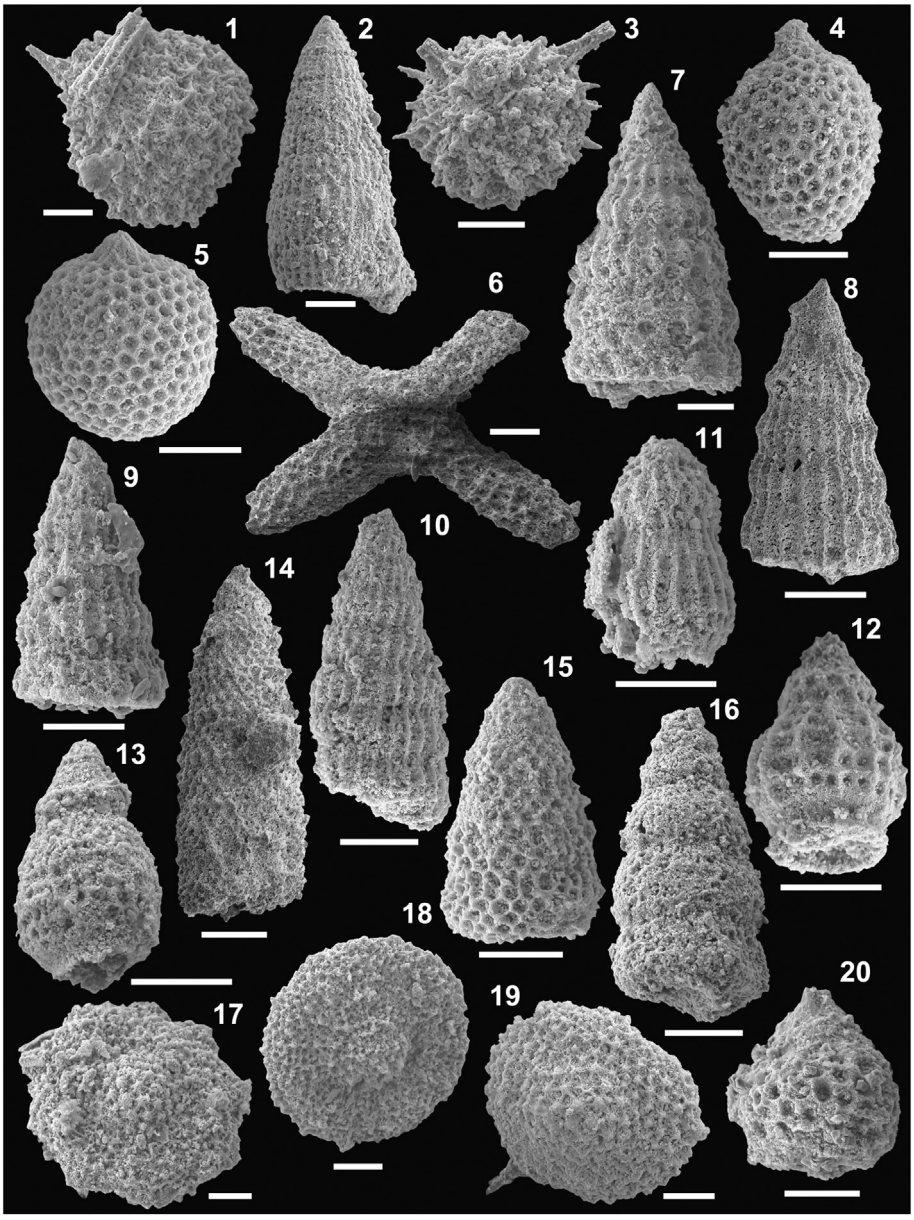

Fig. 11. Scanning Electron Microscope (SEM) images of selected radioalaria taxa (scale bar 50 μm). (1) *Alievium* sp. cf. *A. murphyi* Pessagno, MK367; (2) *Archaeodictyomitra* sp. cf. *A. regina* Campbell and Clark, MK469; (3) *Becus* (?) sp., MK367; (4) *Cryptamphorella macropora* Dumitrica, MK367; (5) *Cryptamphoraella sphaerica* (White), MK367; (6) *Crucella* sp. cf. *C. messinae* Pessagno, MK367; (7) *Dictyomitra formosa* (Squinabol), MK367; (8) *Dictyomitra* sp. cf. *D. formosa* (Squinabol), MK367; (9) *Dictyomitra* sp. cf. *D. formosa* (Squinabol), MK469; (10) *Dictyomitra* sp. cf. *D. multicostata* Zittel, MK469; (11) *Dictyoprora sallilum* (Foreman), MK367; (12) *Dictyoprora urna* (Foreman), MK367; (13) *Dictyoprora urna* (Foreman), MK469; (14) *Foremanina* (?) sp., MK367; (15) *Parvimitrella* sp. cf. *P. mediocris* (Tan) sensu O'Dogherty (1994), MK367; (16) *Parvimitrella* sp., MK469; (17) *Pseudoaulophacus parguerensis* Pessagno, MK367; (18) *Pseudoaulophacus* sp. cf. *P. lenticulatus* (White), MK367; (19) *Pseudoaulophacus* sp. cf. *P. putahensis* Pessagno, MK367; (20) *Rhopalosyringium* sp., MK367.

Y, Sc, Nb, Hf, and Th), as well as some transition metals (e.g., Ni, Co, Cr, and V) are considered to be relatively immobile during low-temperature alteration and metamorphism (Cann, 1970; Pearce and Norry, 1979). For these reasons, the geochemical features of the Durkan Complex volcanic rocks will be described here using only immobile element compositions.

The volcanic rocks taken in the different transects show relatively uniform geochemical features (Table 1). In other words, no geochemical variation in volcanic rocks can be observed in the different transect. In fact, they consist of alkaline basaltic rocks, as testified by the high Nb/Y ratios (Table 1, Fig. 12). They are characterized by relatively high TiO_2 (2.01–4.61 wt.%), P_2O_5 (0.30–1.10 wt.%), Zr (154–478 ppm), Nb (21–68 ppm) and Th (2–9 ppm) contents coupled with relatively low Y abundance (17–25 ppm). The contents of Ni, Co, Cr, and V are variable, but generally they are relatively low (Table 1). For example, Cr content range from 2 ppm to 412 ppm, but most samples show Cr contents within the 40–140 ppm. Likewise, V content ranges from 124 ppm to 406 ppm, but most samples have V values between 170 ppm and 300 ppm. The Durkan Complex basalts show relatively high Ti/V and Zr/Y ratios, as well as relatively low Zr/Nb ratios (Table 1). These ratios are extremely different from those of the N-MORB (normal-type mid-ocean ridge basalt, e.g., Zr/Y = 2.64; Zr/Nb = 31.8) of Sun and McDonough (1989), whereas they are comparable with oceanic island alkaline basalts (in the OIB of Sun and McDonough, 1989; Zr/Y = 9.66; Zr/Nb = 5.83; see also Shervais, 1982; Pearce, 1996). N-MORB normalized incompatible elements show patterns, which are regularly decreasing from Rb to Y (Fig. 13). Durkan Complex basalts show both patterns and relative elemental abundance that are very similar to

Table 1
Major (wt.%) and trace (ppm) composition of basaltic rocks from the western Durkan Complex. The transect and the lithostratigraphic unit from which samples were collected are shown. The petrographic texture is also reported for each sample.

Transect	Manujan	Manujan	Chah Shahi 1	Chah Shahi 1	Chah Shahi 1	Chah Shahi 1	Chah Shahi 2	Chah Shahi 2	Zandan	Zandan	Zandan
Lithostratigraphic unit	Chert & Cherty Lim.	Chert & Cherty Lim.	VSC	Chert & Cherty Lim.	VC	VSC	VC	VCS	Meta VC	VSC	VSC
Sample	MK365	MK370	MK493	MK373	MK491	MK496	MK859	MK855	MK479	MK907	MK 894
Texture	aph	aph	dol	aph	dol	prh	prh	aph	aph	aph	aph
Succession Type	Type I	Type I	Type II	Type I	Type II	Type II	Type II	Type II	Type III	Type III	Type III
Note	Pillow	Pillow	MLF	Pillow	MLF	MLF	MLF	MLF	MLF	Pillow	Pill. brec.
XRF analyses											
SiO_2	51.40	51.84	47.62	48.19	44.34	46.72	42.06	45.10	51.69	51.84	51.77
TiO_2	2.27	2.27	2.01	2.72	2.25	3.41	3.41	3.28	3.06	4.61	3.41
Al_2O_3	14.81	16.40	16.67	14.33	14.31	15.16	13.14	12.83	13.91	14.19	14.77
Fe_2O_3	1.24	1.27	1.46	1.39	1.74	1.36	1.69	1.49	1.42	1.39	1.329
FeO	8.28	8.44	9.75	9.30	11.60	9.09	11.26	9.92	9.49	9.28	8.86
MnO	0.09	0.17	0.16	0.13	0.14	0.17	0.16	0.14	0.14	0.32	0.19
MgO	5.11	5.03	5.50	6.35	14.08	9.88	11.82	8.39	7.30	3.39	4.06
CaO	6.70	5.21	9.04	8.47	5.75	8.63	10.17	11.97	5.61	6.08	8.72
Na_2O	5.78	4.05	2.70	3.55	1.67	2.79	0.91	1.75	2.93	5.50	4.75
K_2O	0.81	1.40	1.28	0.38	0.44	0.25	1.80	1.79	0.29	1.08	0.54
P_2O_5	0.47	0.43	0.34	0.35	0.30	0.55	0.40	0.54	0.35	1.10	0.79
LOI	2.69	3.43	3.03	4.27	3.13	1.62	3.14	2.66	3.51	1.11	0.43
Total	99.66	99.94	99.56	99.45	99.76	99.65	99.97	99.87	99.71	99.89	99.62
Mg#	52.4	51.5	50.1	54.9	68.4	66.0	65.2	60.1	57.8	39.4	45.0
Zn	170	118	106	105	122	72	90	60	126	97	104
Cu	59	75	125	93	116	102	108	125	44	33	10
Sc	26	30	24	23	27	20	34	24	27	12	12
Ga	17	19	21	16	18	11	19	16	15	13	16
Ni	47	101	32	51	356	66	134	53	70	33	b.d.l.
Co	61	53	42	42	67	40	63	48	32	37	27
Cr	143	259	51	92	412	85	280	42	193	3	2
V	230	173	227	268	294	336	373	406	267	124	130
Ba	219	186	277	161	204	1210	370	267	135	182	421
Pb	2	3	2	3	2	2	3	2	2	2	3
Rb	20	27	30	7	8	6	24	36	6	40	21
Sr	724	419	537	342	837	570	591	659	113	188	318
Y	24	25	24	25	22	17	18	19	21	21	19
Zr	194	222	154	291	192	313	295	320	229	478	358
Nb	25	26	23	36	27	70	62	62	31	68	44
La	19	20	16	27	21	55	44	45	20	42	25
Ce	42	54	37	70	66	129	121	119	60	93	74
Nd	19	20	17	32	27	27	40	44	29	36	37
Hf	4	4	6	6	6	8	7	8	5	6	7
Th	2	2	2	4	3	7	8	5	3	9	5
Nb/Y	1.05	1.03	0.97	1.47	1.22	4.12	3.41	3.23	1.52	3.23	2.29
Ti/V	61	82	55	64	48	62	57	50	71	225	159
Zr/Y	8.12	8.94	6.51	11.9	8.59	18.4	16.1	16.7	11.2	22.6	18.8
Zr/Nb	7.76	8.69	6.70	8.05	7.02	4.47	4.73	5.17	7.35	7.01	8.23

Abbreviations: Lim. – Limestones; VSC – Volcano-Sedimentary Complex; VC – Volcanic Complex; bas – basalt; aph – aphyric texture; dol – doleritic texture; prh – porphyritic texture; MLF – massive lava flow; pill. brec. – pillow breccia. Mg# = 100 × MgO / (MgO + FeO). Fe_2O_3 = 0.15 × FeO.

those of alkaline OIB (Sun and McDonough, 1989) and typical P (plume type)-MORB from the South West Indian Ridge (Janney et al., 2005). Accordingly, in the discrimination diagram shown in Fig. 14, the Durkan Complex basalts plot in the field for subduction-unrelated oceanic setting and, particularly, in the compositional field shared by the typical P-MORB and alkaline OIB.

5.3. Vesicles content

In Section 5.1, we outlined that some of the Durkan Complex basaltic rocks exhibit amygdaloidal texture. In volcanic rocks, the vesicles content per volume varies as a function of several factors, including the chemical affinity of the magma, its volatiles content and their dissolution within the magma, as well as the water depth of eruption (Moore, 1970; Moore and Schilling, 1973; Memtimin et al., 2019). Among these factors, the magma affinity and water depth of eruption are believed to be strictly related (Moore, 1970). In fact, the alkaline volcanic rocks are generally more vesicles-rich than those of tholeiitic chemical affinity, at a given eruption depth (Fig. 15). In addition, in both alkaline and tholeiitic volcanic rocks the increase of vesicularity is related to the decrease of the eruption depth (Fig. 15; Moore, 1970; Moore and Schilling, 1973; Memtimin et al., 2019). Our geochemical data shown in Section 5.2 indicate that the Durkan Complex magmatic rocks have alkaline affinity and quite comparable geochemical features. Therefore, the main parameter influencing the vesicles content can be assumed as related to the depth of eruption. Given these data, we performed a comparative estimation of the vesicles per volume choosing samples associated with different sedimentary successions, which, in turn, indicate different depth of sedimentation (Fig. 15). The results show that the basaltic sample MK894 from the Volcano-Sedimentary Sequence, which is overlaying by the platform-derived Massive Limestone (Fig. 3a2), is characterized by a high amount of vesicles (~ 38%). This suggests eruption in shallow-water environment (Fig. 15). On the contrary, the basaltic sample MK365 is interlayered with the pelagic

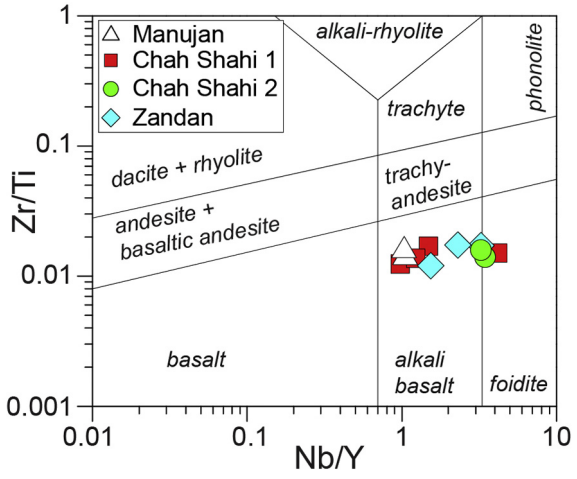

Fig. 12. Nb/Y vs. Zr/Ti discrimination diagram of Winchester and Floyd (1977) modified by Pearce (1996) for basaltic rocks from the western Durkan Complex.

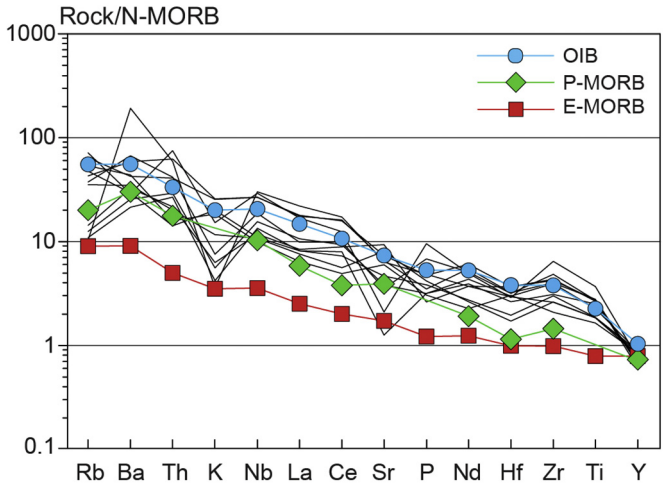

Fig. 13. N-MORB normalized incompatible element patterns for basaltic rocks from the western Durkan Complex. Normalizing values are from Sun and McDonough (1989).

succession of the Cherty-Limestone and Basalt lithostratigraphic unit (Fig. 3b3) and is characterized by a significantly lower percent of vesicles per volume (MK365, ~ 2%). This evidence indicates eruption in deep-water environment (Fig. 15). Finally, the basaltic sample MK496 from the Volcano-Sedimentary Sequence in the tectonic slice of Fig. 3c2 is stratigraphically associated to pelagic limestone and shows a vesicles content per volume of ~16%, suggesting a relatively deep-water eruption environment (Fig. 15).

6. Discussion

6.1. Reconstruction of the stratigraphy of the western Durkan Complex

The integration of the stratigraphic and biostratigraphic data from different transects allows us to identify three main types of stratigraphic successions in the western Durkan Complex, which hereafter will be named as Type-I, Type-II and Type-III (Fig. 16). Basalts with alkaline geochemical affinity occur within all the three types of successions (Section 5.2) and are associated with Late Cretaceous sedimentary rocks (Fig. 16). The geochemistry of the Durkan Complex basalts is compatible with their genesis in a within-plate oceanic setting.

6.1.1. Type-I stratigraphic succession

The Type-I succession is defined based on the stratigraphic features of the Cherty-Limestone and Basalt lithostratigraphic unit, which is preserved in the tectonic slice of the Manujan transect, as well as in the structurally lowermost tectonic slice of the Chah Shahi 1 transect (Fig. 3c3). It consists of a pelagic sequence including reddish cherts and pinkish- to whitish cherty-limestones alternated with reddish shales as well as marls and silty-marls (Fig. 16). The integration of radiolarian, foraminifera and nannoplacton biostratigraphic data from the different tectonic slices indicates Coniacian–early Campanian age for this succession (Fig. 16). In addition, basaltic lava flows and less abundant volcaniclastic arenites are interbedded within the pelagic succession (Fig. 16). The low vesicularity of the lava flows within the Cherty-Limestone and Basalt lithostratigraphic unit (Fig. 15) suggest the eruption in a deep-marine environment with a relatively thick water column pressure (Moore, 1970; Moore and Schilling, 1973). All these data support the emplacement of the magmatic rocks in a pelagic depositional setting during the Coniacian–early Campanian age.

6.1.2. Type-II stratigraphic succession

The Type-II stratigraphic column (Fig. 16) has been reconstructed by integrating the stratigraphic features of the two uppermost tectonic slices of the Chah Shahi 1 transect (Fig. 3c1, c2), the uppermost tectonic slice of the Chah Shahi 2 transect (Fig. 3d5), as well as some tectonic slices in the thrust zone of the Chah Shahi 2 transect (Fig. 3d1–d3). These tectonic slices are characterized by stratigraphic successions showing comparable stratigraphic features, which are: (i) a basal Volcanic Sequence passing upward to a Volcano-Sedimentary Sequence; (ii) a pelagic and hemipelagic sequences (i.e., Limestone and Shale, and Cherty-Limestone and Varicoloured Shale lithostratigraphic units) resting above the Volcano-Sedimentary Sequence; (iii) different types of mass-transport deposits interlayered at different stratigraphic levels (Fig. 16). In the tectonic slices within the thrust zone of the Chah Shahi 2 transect only the basal part of Type-II succession occurs most likely as a consequence of the tectonic deformation. The Volcanic Sequence and the Volcano-Sedimentary Sequence show transitional stratigraphic relationships, as suggested by the occurrence in both complexes of: (i) basalts showing comparable intra-plate geochemical affinity (Section 5.2); and (ii) volcaniclastic breccias as well as volcaniclastic arenites. Following the diagnostic criteria proposed by McPhie et al. (1993), Fisher (1984), and Gutierrez et al. (2006), these sedimentary rocks could be defined as volcanogenic deposits and they likely represent the results of gravity-induced high density sedimentary processes (e.g., rock fall, grain flows, cohesive debris flows, hyperconcentrated flows, and/or high density turbiditic currents) operating on pre-existing volcanic series and/or volcanic reliefs. The volcaniclastic rocks become abundant in the Volcano-Sedimentary Sequence where they are interlayered with limestones, shales, and breccias showing a mixed carbonatic-volcanic composition of both clasts and matrix (Fig. 16). These breccias likely represent the sedimentary products of mass-transport processes sourced from coeval volcanic and carbonatic debris. The limestones from the Volcano-Sedimentary Sequence in the Chah Shahi 1 transect exhibit Cenomanian pelagic foraminifera assemblages (Fig. 16), indicating relatively deep-water depositional setting for this Sequence. This evidence is further supported by the analyses of vesicles contents of volcanic rocks from the Volcano-Sedimentary Sequence, which indicates eruption in relatively deep-water environment. The Type-II succession continues with a pelagic and hemipelagic sedimentary sequence (Fig. 16), whose stratigraphic features are defined on the basis of the succession of the Limestone and Shale, and Cherty-Limestone and Varicoloured Shale lithostratigraphic units

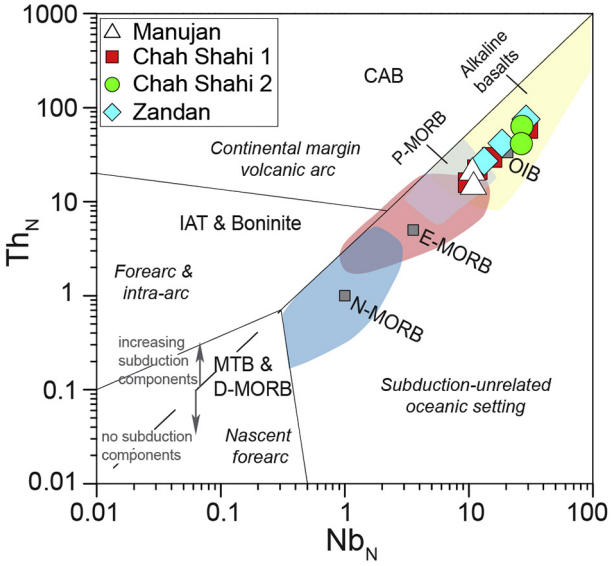

Fig. 14. N-MORB normalized Th vs. Nb discrimination diagram of Saccani (2015) for basaltic rocks from the western Durkan Complex. Abbreviations: MORB, mid-ocean ridge basalt; N-, normal type; E-, enriched type; D-, depleted type; IAT, island arc tholeiite; CAB, calc-alkaline basalt; OIB, alkaline oceanic within-plate basalt; MTB, medium titanium basalt. Normalizing values, as well as the composition of typical N-MORB, E-MORB, and OIB (grey stars) are from Sun and McDonough (1989).

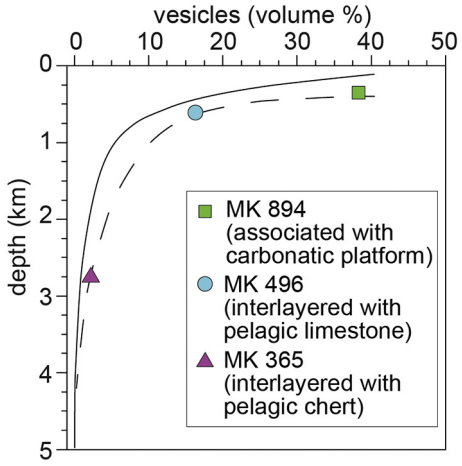

Fig. 15. Relationship between water depth of eruption and vesicles content for the western Durkan Complex magmatic rocks. The different curves indicate the depth-vesicles percent for tholeiitic (solid line, from Moore and Schilling, 1973) and alkaline (dashed line, from Moore, 1970) volcanic rocks. The sedimentary rocks associated with each sample is also indicated for a better comparison of the depth of eruption deduced from the vesicles content with the sedimentary rocks paleo-depth indicators.

(Fig. 3c1, c2, d5). Although these two lithostratigraphic units display some minor differences, they are comparable for: (i) the occurrence of pelagic limestones and pinkish to whitish cherty limestones interlayered with shales; (ii) the stratigraphic position above the Volcano-Sedimentary Sequence; (iii) the occurrence of calcareous turbidites and abundant carbonatic breccias and minor volcaniclastic arenites (Fig. 16). Unfortunately, the limestone from Limestone and Shale and the Cherty-Limestone and Varicoloured Shale underwent high degree of diagenetic and/or metamorphic recrystallization, hampering a biostratigraphic age determination. However, their stratigraphic position and their microfacies comparable with the Cenomanian limestones of the Volcano-Sedimentary Sequence suggests a latest Cenomanian or younger age (Fig. 16).

6.1.3. Type-III stratigraphic succession

The type III succession (Fig. 16) has been reconstructed from the integration of the stratigraphic features of the different successions preserved in the two tectonic slices of the Zandan transect (Fig. 3a), as well as within a slice of the thrust zone in the Chah Shahi 2 transect (Fig. 3d4). The structurally lowermost slice of the succession in the Zandan transect is metamorphosed under subgreenschist facies conditions as indicated by paragenesis of the metamorphic foliation in the meta-basalts; nonetheless, the stratigraphic features are fairly well preserved. The Massive Marble and the platform-derived Massive Limestone lithostratigraphic units (Fig. 16) could be correlated and they most likely represent comparable platform successions deformed at different depth into the accretionary wedge. In fact, as shown in Section 3.2.1, their correlation is suggested by: (i) their similar lithostratigraphic architecture; (ii) the occurrence of volcaniclastic debris in both the lithostratigraphic units; (iii) their similar stratigraphic position above a volcanic stratigraphic interval, represented by the same alkaline volcanic rocks (Fig. 3a1, a2). The biostratigraphic data indicate a Cenomanian age for the platform-derived Massive Limestone (Fig. 16). This age can possibly be extended to the Massive Marble lithostratigraphic unit from both the lower slice of the Zandan transect and the tectonic slice within the thrust zone in the Chah Shahi 2 transect (see Fig. 3a1, d4), whose metamorphism hamper any age determination. However, it is not possible to exclude that the Massive Marble facies could represent a platform succession of different ages. In the metamorphic and non-metamorphic successions of the Zandan transect, the platform successions stratigraphically overlie the Meta Volcanic Sequence and the Volcano-Sedimentary Sequence, respectively (Fig. 3a1, a2). The occurrence in both sequences of volcaniclastic and volcanic rocks, the comparable geochemistry of their volcanic rocks, and their stratigraphic relationship between the overlaying platform successions seems suggest both lateral and vertical stratigraphic transition between the two complexes (Fig. 16). In addition, lateral facies variation in the depositional basin before the onset of the platform sedimentation are further suggested by the occurrence in the Volcano-Sedimentary Sequence of massive limestone as well as mixed calcareous-volcanic turbidites. In the metamorphic slice of the Zandan transect, the platform succession of the Massive Marble lithostratigraphic unit is followed by the Meta Cherty-Limestone and Shale, which shows a thinning upward trend. This lithostratigraphic unit likely represents a hemipelagic and pelagic succession indicating the drowning of the carbonatic platform (Fig. 16, see also Fig. 3a1). The non-metamorphic equivalent of this lithostratigraphic unit does not occur above the Massive Limestone, possibly as a consequence of a depositional hiatus or the elision for the tectonic deformation within the Makran Accretionary Prism. Unfortunately, due to the high metamorphic recrystallization of the limestone no biostratigraphic data are up to now available for the succession of the Meta Cherty-Limestone and Shale lithostratigraphic unit. However, its stratigraphic position (i.e., above the Massive Marble succession correlated with the Cenomanian platform succession of the Massive Limestone) suggests a Late Cretaceous age for this lithostratigraphic unit (Fig. 16).

6.2. Stratigraphic implications for the regional geology of the North Makran

The different types of succession of the Durkan Complex in the western sector of the North Makran record a complex interplay between sedimentation and alkaline magmatism during the Late Cretaceous. Unfortunately, in the western Durkan Complex the Late Cretaceous successions have been tectonically detached from their "basements" during their tectonic deformation in the Makran accretionary wedge. Nonetheless, it is worth to note that extremely subordinated tectonic slices showing Permian successions occur in the western Durkan Complex and they show tectonic relationship with the Cretaceous succession (McCall, 1985). This author has interpreted the Permian tectonic slices as the original stratigraphic base of the Cretaceous succession, though

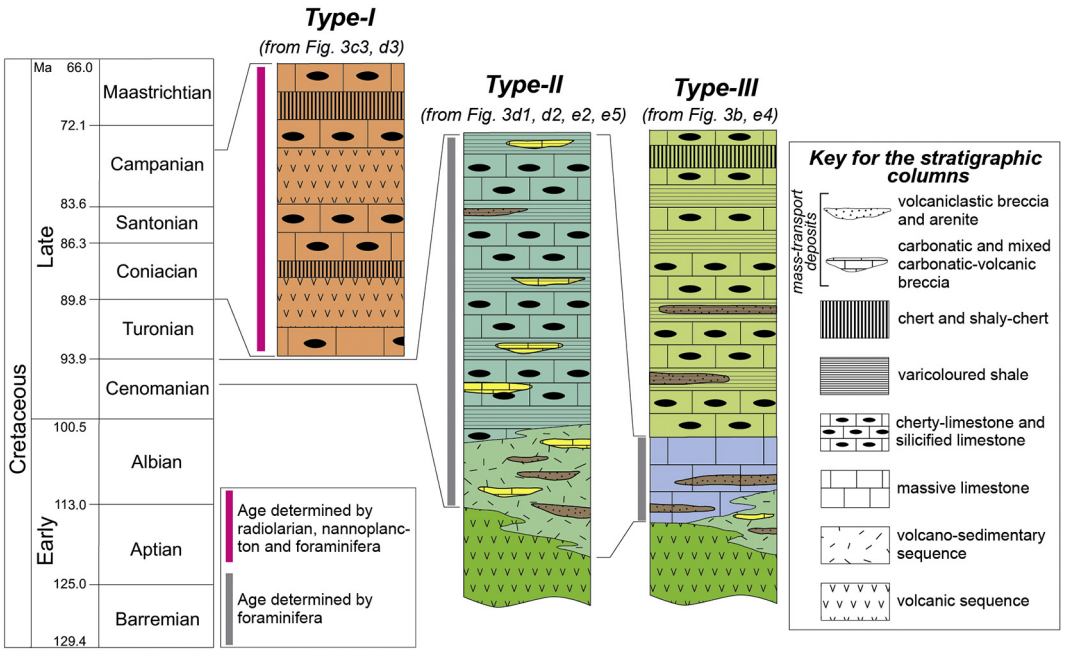

Fig. 16. Schematic reconstructed stratigraphic column and ages for the three different types of succession in the western Durkan Complex.

clear stratigraphic relationships were not observed. Therefore, this hypothesis should be re-investigated.

Fig. 17 shows the tectono-sedimentary and magmatic stages recorded by the succession of the western Durkan Complex (this work) and those proposed in literature for the eastern part of the Durkan Complex (Hunziker, 2014; Hunziker et al., 2015). According to Hunziker et al. (2015), pre-Cretaceous rock assemblages are exposed in the eastern part of the Durkan Complex (i.e., Remeshk - Fannuj area). These authors reconstructed the Middle Jurassic–Early Cretaceous extensional history that affected the southern margin of the Lut block (i.e., the Eurasian margin; Fig. 17; McCall and Kidd, 1982; Burg, 2018; see also Hunziker et al., 2015 and Fig. 14 therein for further detail). This extensional tectonic led to the separation of the Bajgan-Durkan microcontinent from the southern margin of the Lut Block, and the subsequent opening of the North Makran Ocean during Early Cretaceous (Hunziker et al., 2015; Burg, 2018). The extensional tectonic stages were characterized by the emplacement of Early - Late Jurassic granitoid bodies into a Jurassic carbonatic platform (Fig. 17). These rocks were subsequently unconformably covered by Early Cretaceous pelagic sediments associated with alkaline and tholeiitic lavas, which indicate the progressive deepening of the depositional setting (Fig. 17). In this scenario, alkaline volcanic rocks in the eastern Durkan Complex represent within plate rift-related magmatism (Fig. 17), as commonly accepted in literature (Robertson, 2007; Pearce, 2008; Saccani, 2015; Saccani et al., 2015).

The comparison of these previously published data and those presented in this work clearly outlines that the rift-related phases recorded in the eastern Durkan Complex are significantly older than the tectono-sedimentary and magmatic phases recognized for the western Durkan Complex (Fig. 17). This rises serious doubt about the interpretation of the western Durkan Complex as remnants of a rifted continental margin domain. In fact, this interpretation implies a laterally diachronous rift of the southern margin of the Lut Block, which would have been active for 70–100 Myr, from Middle Jurassic to Late Cretaceous (Fig. 17). This scenario seems to be quite unreasonable and it is in contrast with the Cretaceous regional-scale evolution of the northern part of the Neo-Tethys realm. In fact, the Late Cretaceous tectono-sedimentary evolution and the alkaline magmatism recorded by the western Durkan Complex post-dates the spreading stages of the North Makran Ocean,

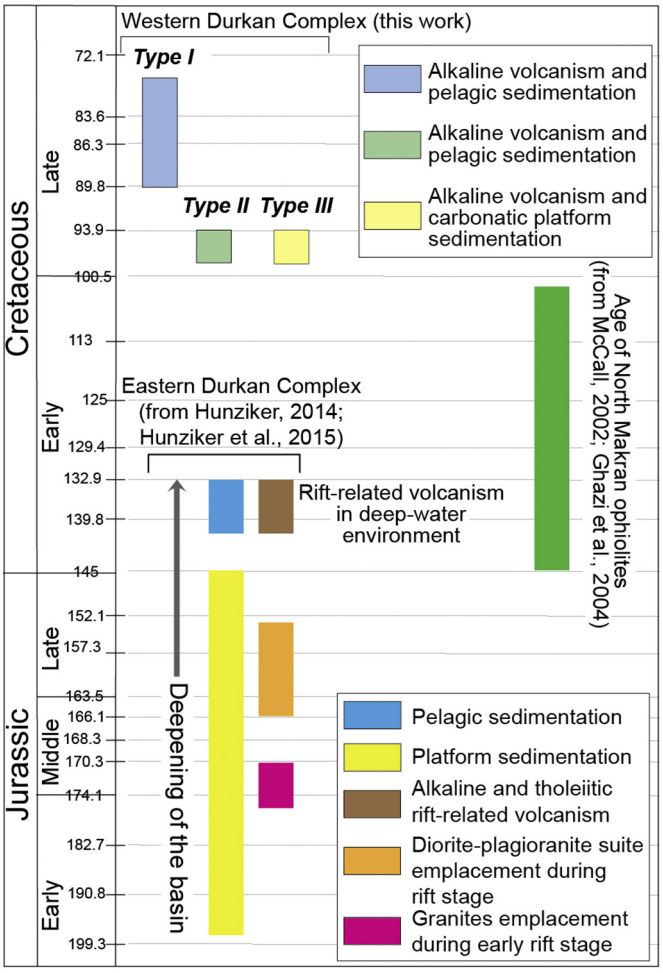

Fig. 17. Comparison of the tectono-sedimentary and magmatic events recorded in the western Durkan Complex (this work) and the eastern Durkan Complex (Hunziker, 2014; Hunziker et al., 2015). Ages of the North Makran Ophiolites are also shown (data source: McCall, 2002; Ghazi et al., 2004).

represented by the Early Cretaceous ophiolitic sequences (Fig. 17 and reference quoted therein). In addition, it is commonly accepted that starting from the Late Jurassic - Early Cretaceous the southern margin of the Eurasian plates (e.g., the Lut block in the Makran transect) was affected by the beginning of convergence kinematic rather than extensional tectonics (Dercourt et al., 1986; Şengör et al., 1988; Agard et al., 2011; Hassanzadeh and Wernicke, 2016; Barrier et al., 2018; Burg, 2018; Saccani et al., 2018; Rolland et al., 2020). This tectonic regime was associated with the northward motion of the Arabian Plate and the beginning of the northward subduction of the Neo-Tethys oceanic lithosphere and its minor branches, such as the North Makran Ocean, below the Eurasia continental margin (Hässig et al., 2013a, 2013b; Monsef et al., 2019; Barbero et al., 2020b; Bonnet et al., 2020a, 2020b). Another clue strongly suggesting that the western Durkan Complex may not represent a continental margin domain is the total lack of continental-derived debris within the clastic deposits. In fact, during the rifting stages the sediment supply of continental margin clastic successions is mainly represented by quartz-rich debris sourced from continental-derived rocks (Robertson, 2007 for exhaustive discussion; Berra et al., 2009; Festa et al., 2020). This kind of deposits is completely lacking in the western Durkan Complex successions, which, on the contrary, include mass-transport deposits showing volcanic, carbonatic, and mixed volcanic-carbonatic composition of the debris, without any kind of continental derived debris. In conclusion, our new data suggest that the stratigraphic successions and the alkaline volcanic rocks of the western Durkan Complex do not represent remnants of a rifted continental margin.

It is widely accepted in literature that alkaline basaltic rocks erupted mainly in within-plate oceanic island setting (Pearce, 2008; Dilek and Furnes, 2011; Safonova and Santosh, 2014; Saccani, 2015; Saccani et al., 2015). Studies of modern oceanic setting indicate that the within-plate alkaline magmatic activity is commonly associated to the rising of mantle plume and/or hot spot magmatism (Morgan, 1971; Pearce, 2008). This magmatic activity results in the formation of volcanic reliefs and/or a chain of reliefs (i.e., seamounts or oceanic islands), which are built on older and pre-existing oceanic lithosphere (Morgan, 1971; Staudigel and Clague, 2010; Dilek and Furnes, 2011). Several recent studies document the occurrence of abundant alkaline magmatic rocks and OIBs within collisional and accretionary belts from Armenia to Himalaya (Rolland et al., 2010, 2020; Hässig et al., 2013a, 2013b; Saccani et al., 2013, 2018; Yang and Dilek, 2015; Azizi et al., 2018; Esmaeili et al., 2019). Significantly, some of these alkaline and OIB rocks are Cretaceous in age and were interpreted as remnants of seamounts and/or oceanic plateau associated with plume-influenced magmatic activities in the northern sector of the Neo-Tethys Ocean at this time (Rolland et al., 2010, 2020; Saccani et al., 2013, 2018; Esmaeili et al., 2019). Therefore, these regional-scale evidences strongly suggest that the Late Cretaceous sedimentary succession associated with alkaline magmatic rock in the western Durkan Complex could represent tectonically disrupted remnants of seamounts and/or oceanic islands, which existed in the northern sector of the Neo-Tethys. The wide age range indicated by biostratigraphic data suggest that this Complex is composed by fragments of distinct seamounts (i.e., a seamount chain) rather than the remnants of a unique seamount. In our interpretation, the Permian successions reported in the western Durkan Complex would represent exotic tectonic inclusions juxtaposed to the Cretaceous successions. Their paleogeographic origin is up to now unknown. Future stratigraphic and biostratigraphic studies on these assumed Permian slices are needed to better constrain their ages and depositional settings. In the following section we compare the stratigraphic record of the Durkan Complex successions with the stratigraphic architecture, volcanic facies as well as sedimentary and volcanic evolution proposed in literature for modern seamounts and oceanic islands in order to test our hypothesis.

6.3. New definition of the Late Cretaceous tectono-sedimentary and volcanic environment for the western Durkan Complex

Data from present-day seamounts and their surrounding aprons have led to the recognition of two main stages of growth of seamounts, namely, the deep-water and the shallow-water shield stages (Staudigel and Schmincke, 1984; Moore and Clague, 1992; Gutierrez et al., 2006; Staudigel and Clague, 2010). The deep-water stage (depths between ~2–3 km; Staudigel and Clague, 2010) is characterized by coeval pelagic sedimentation and non-explosive volcanic activity across and onto older oceanic crust and/or its sedimentary cover (Staudigel and Schmincke, 1984). This activity results in sills and dykes intruding the older crust and in a number of small coalescent volcanic reliefs formed by pillow lava flows, and less abundant pillow breccias and volcaniclastic rocks along the relatively slightly inclined flanks. In contrast, the shallow-water shield stage is marked by the seamount growth up to reach, at its summit, the critical depth for drastic increase in exsolution of magmatic volatiles (~ 700 of water-depth or less), which, in turn, results in explosive eruptions and/or subaerial eruptions in seamount emerged above the sea-level (Staudigel and Schmincke, 1984; Moore and Clague, 1992; Gutierrez et al., 2006; Staudigel and Clague, 2010). The changing in the eruption style and the growth of the seamount cause: (i) the significant increase of clastic volcanic and volcaniclastic rocks as a consequence of explosive volcanism and (ii) the differentiation of seamount summit, seamount flanks, and deep-water apron depositional settings (Staudigel and Schmincke, 1984; Staudigel and Clague, 2010; Saint-Ange et al., 2013). The summit is characterized by shallow-water volcanic facies, such as highly vesicular pillow lava flows, pillow breccias, subaerial lava flows and pyroclastic deposits (Staudigel and Schmincke, 1984), and eventually by carbonatic platform deposits (Moore and Clague, 1992). In contrast, the flanks and their surrounding deep-water apron are mainly characterized by the deposition of volcaniclastic mass-transport deposits, as response of the steepening of the seamount flanks and the gravitational instability of volcanic debris produced by explosive volcanism (Gutierrez et al., 2006; Saint-Ange et al., 2013; Quartau et al., 2018). In addition, lava flows and intrusions may occur in the flanks because of the downslope emplacement of flows from the summit and/or volcanic activity in minor eruptive centres along the flanks (Staudigel and Schmincke, 1984).

The stratigraphic features of the Type-I succession and their comparison with modern oceanic settings likely suggest that it represents the remnants of the deep-water stages of formation of a seamount (Fig. 18a). In fact, Type-I succession records sedimentation and volcanic activity in a deep-water setting below a thick water column. The minor occurrence of pillow breccias and thin volcaniclastic arenites would suggest the fragmentation and gravitational instability of basaltic lava flows along morphological relief(s), which were probably characterized by rather low inclination and little elevation (Fig. 18a). These reliefs were likely represented by some, but rather small in elevation, coalescent volcanic cones, which were formed by non-explosive and submarine basaltic volcanic activity (Fig. 18a). However, the relatively low abundance of pillow breccias and volcaniclastic arenites and their limited thickness compared to the basaltic lava flows suggest a depositional environment in which the gravity-driven sedimentary processes were subordinate (Fig. 18a) that is well comparable with the environment proposed for deep-water stage of growth of modern seamount (Staudigel and Schmincke, 1984).

The stratigraphic characteristics of the Type-II succession are well comparable with those of seamount flank settings forming in the shallow-water shield stage, as indeed observed in modern seamounts, as described above (Fig. 18b). In fact, Type-II succession records volcanic activity, pelagic sedimentation, as well as gravity-induced sedimentary processes in relatively deep-water depositional setting. The abundant occurrence of mass-transport deposits indicates that the depositional

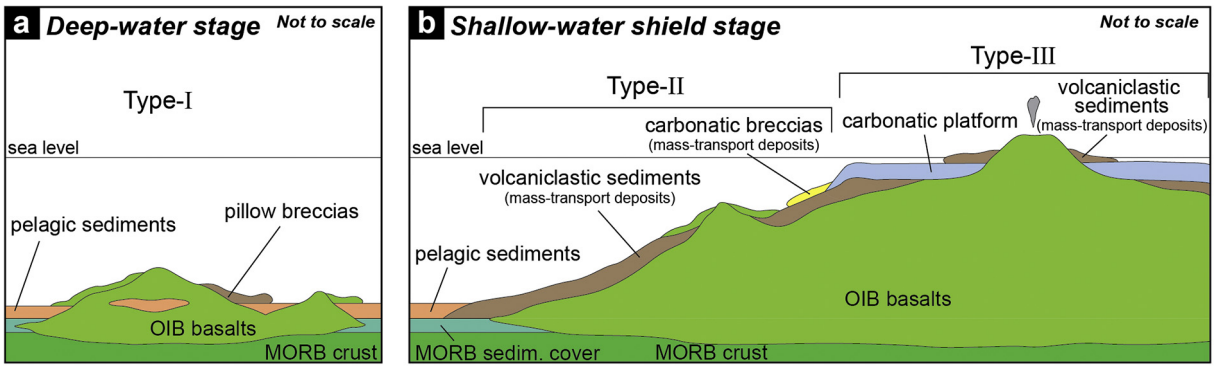

Fig. 18. Schematic reconstruction of the depositional and eruptive setting of the Cretaceous successions of the western Durkan Complex during the deep-water stage (a) and the shallow-water shield stages (b).

basin was influenced by morphological relief(s), which, according to the composition of mass-transport deposits, were characterized by heterogeneous volcanic and carbonatic rocks and/or unconsolidated carbonatic sediments (Fig. 18b). These reliefs likely corresponded to the flank and summit of the seamount, onto which a great amount of unconsolidated volcanic debris is produced by the explosive magmatism (Fig. 18b). In addition, in the seamount summit carbonatic platform sedimentation resulted in the production of carbonatic debris. All these material is prone to be resedimented by gravity flows along the flanks and in the deep-water apron at their base as a consequence of gravitational instability, possibly induced by both volcanic activity and the flanks steepening (Fig. 18b).

The stratigraphic features of the Type-III succession are comparable with the sedimentary and volcanic facies observed in seamount summit settings during the shallow-water shield stage (Fig. 18b). Indeed, Type-III succession records shallow-water carbonatic platform sedimentation and rather explosive volcanic eruptions under a relatively thin water column (Fig. 18b). In addition, the occurrence of volcaniclastic arenites interbedded within the platform sequence suggests the existence of exposed volcanic rocks and their sedimentary remobilization during platform deposition (Fig. 18b). During the shallow-water shield stage, the seamount summit is characterized by laterally heterogeneous articulated depositional setting, as response of the interplay with the rate of the volcanic activity and its later migration, the platform sedimentation, and the erosion of pre-existing volcanic cones (Staudigel and Schmincke, 1984; Gutierrez et al., 2006; Saint-Ange et al., 2013). This, again, agrees with the stratigraphic features of the Type-III succession, which record interplay between volcanic activity, platform sedimentation and remobilization of volcanic debris along exposed volcanic relief (Fig. 18b). Finally, the upper part of the Type-III succession is characterized by hemipelagic and pelagic sequences, which stratigraphically rest above the Cenomanian carbonatic platform (Fig. 16). This evidence suggests that platform built on top of the seamount summit were progressively drowned, as commonly observed in modern oceanic island settings in response of a combination of several factors (e.g., ceasing volcanic activity, isostatic subsidence, erosion and collapse of seamount/s, global variation of sea level, see Moore and Clague, 1992; Staudigel and Clague, 2010). After their drowning, the seamount summit and flanks were draped by pelagic and hemipelagic deposits with minor intercalation of volcaniclastic arenites, similarly to what is observed in the stratigraphic record of the Type-III succession.

6.4. The role of seamount accretion in controlling the physiography and tectonic evolution of the Makran convergent margin

The entering of a seamount in the subduction complex can strongly influence the deformative processes operating in the frontal prism, as well as the anatomy of the whole convergent margin. For instance, it can produce: (i) the reducing of the accretion and the enhancing of tectonic erosion of the basal part of the prism (Ranero and von Huene, 2000; Bangs et al., 2006; Clarke et al., 2018); (ii) significant deformation of the upper plate, causing uplift and shortening of the already formed accretionary prism and the forearc-arc setting (Lallemand and Le-Pichon, 1987; Lallemand et al., 1989; Dominguez et al., 1998); (iii) the blocking of the subduction zone causing its change in polarity and/or its seaward subduction jump (Rolland et al., 2010; Kerr, 2014; Saccani et al., 2018); (iv) gravitational instability of the frontal part of the subduction complex (e.g., von Huene et al., 2004a, 2004b; Ruh, 2016). In addition, convergence rate is believed to play a significant role in controlling the type and shape of frontal prisms (Clift and Vannucchi, 2004; Malatesta et al., 2013). In detail, slow convergence velocity (< 6 cm/yr) enhances the accretion, whereas high convergence rate (> 6 cm/yr) favour the tectonic erosion processes (Clift and Vannucchi, 2004; Malatesta et al., 2013).

The new data show that the different tectonic slices recognized in the western Durkan Complex represent remnants of the tectonic disruption of Late Cretaceous seamount and/or seamounts chain, which occurred during their incorporation in the Makran Accretionary Prism. In this interpretation, these seamounts were existing at this age in the northern sector of the Neo-Tethys. Here, it is presented a conceptual model for the processes responsible for this tectonic process (Fig. 19a–c). In the first stage, the accretionary wedge is formed from the accretion of fragments of the subducting oceanic lithosphere and its sedimentary cover, whereas the seamount chain is not yet involved in the deformation front (Fig. 19a). This stage was possibly characterized by the prevalence of subduction of oceanic lithosphere rather than accretion at shallow level of the wedge. The entering of the seamount chain in the subduction complex can likely change the deformation style within the frontal prism, enhancing the accretionary processes (Fig. 19b). The landward-side of the seamounts chain was accreted at different depth in the accretionary wedge (A in Fig. 19b). This process produced the progressive imbrication of several tectonic slices formed by different seamount-related successions (Fig. 18 and A, B, C in Fig. 19b). However, the entering in the subduction zone of extremely wide and high seamounts can also cause temporary and laterally variable re-organization of the shape and size of the frontal prism and/or collisional-like deformation of the already formed prism and the forearc region (Cloos, 1993). The evidence that part of the Durkan seamount chains was high enough to be covered by shallow-water platform succession suggests that the entering in the prism of the highest part of a seamount chain (B in Fig. 19b) can cause a shortening of the whole margin, the imbrication of the previously accreted units, as well as of the forearc-arc (Fig. 19b). Ultimately, these processes led to the growth of the frontal prism above a critical taper angle, which triggered the shift from tectonic accretion to erosion of the prism and related gravitational-induced deformation, in order to maintain its dynamic

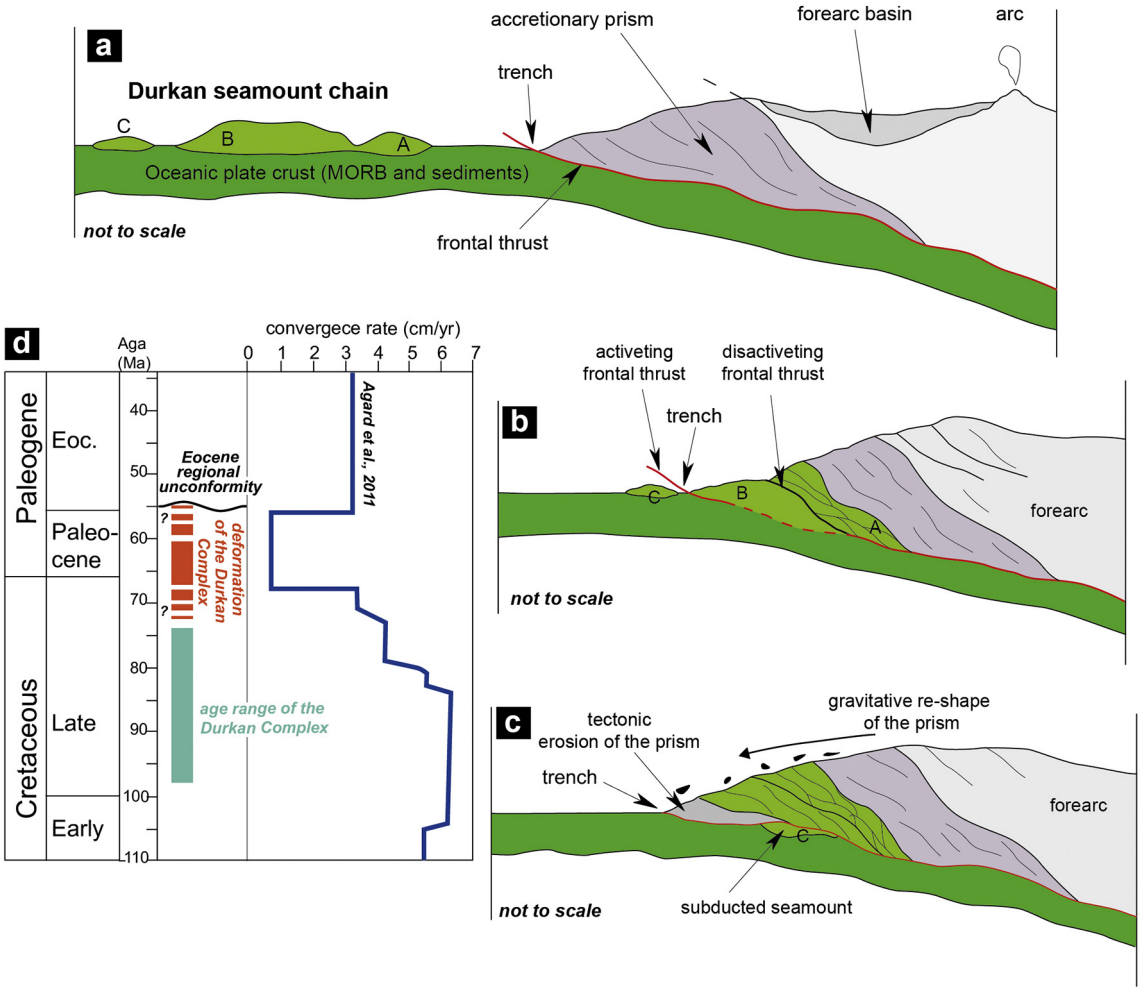

Fig. 19. Conceptual model for the accretion of the Durkan seamount chain in the Makran Accretionary Prism: (a) pre-accretion stage; (b) accretion stage (imbrication of the prism); (c) post-accretion stage and tectonic erosion of the prism. (d) variation of plate convergence rate for the Arabia-Africa and Eurasia during the Late Cretaceous and Early Paleogene (from Agard et al., 2011) and its comparison with time of deformation of the Durkan Complex. Capital letters in panel (a), (b), and (c) indicate different parts of the Durkan seamount chain deformed in different times in the accretionary prism, as discussed into the text.

equilibrium (Fig. 19b, c). In fact, tectonic erosion of the prism and gravitational deformation are believed to represent the most effective processes to react to the overgrowth of the frontal prism (von Huene and Lallemand, 1990, von Huene et al., 2004a, 2004b; Ranero and von Huene, 2000; Marroni and Pandolfi, 2001). As a consequence, the final stages of the collision of the Durkan seamount chain and the frontal prism can possibly be characterized by both basal erosion of the already accreted seamount fragments and gravitational instability of the frontal part of the prism (Fig. 19c).

Unfortunately, the new data presented together with those already published do not allow to properly constrain the absolute chronology of the described tectonic events. In fact, the age of very low-grade the metamorphism is difficult to be constrained by radiometric dating. Similarly, biostratigraphic data are still too absent as biostratigraphic marker are in general poorly preserved for the diagenetic recrystallization and low-grade metamorphism. The only available data to propose chronological constraints for the deformation of the Durkan Complex are the youngest age observed in its stratigraphic succession (i.e., late Campanian) and the oldest age of the deposits unconformably lying above it (i.e., early Eocene; Fig. 19d). According to these data, the incorporation of the Durkan seamount chain in the Makran Accretionary Prism most likely occurred from the latest Cretaceous (i.e. Maastrichtian) to Paleocene or earliest Eocene (Fig. 19d). The probable age for the collision of the Durkan seamount coincides with a significant variation of the plate convergence rate in the Neo-Tethys realm (Fig. 19d). In fact, the late Maastrichtian - early Paleocene time span was characterized by very low convergence rate (< 1 cm/a) between the Arabia and Eurasia plates (Fig. 19a; see also Agard et al., 2011; Barrier et al., 2018). In many cases worldwide, the entry of seamounts and/or oceanic plateaux in the subduction zone significantly lowered the plate convergence rate (see Kerr, 2014 for an exhaustive review). Similarly, the lowering of the convergence rate in the Neo-Tethys observed at regional scale at the same time of the Durkan seamount (s) collision (Fig. 19d) suggests that this collisional event may have played a major role in controlling the convergence rate and the deformation style at the northern margin of the Neo-Tethys Ocean. Further investigations are however needed to better constrain this hypothesis.

7. Conclusion

The Durkan Complex is one of the major tectonic elements of the North Makran domain (Makran accretionary prism, SE Iran) and, though poorly studied, it has been commonly interpreted as a continental margin succession. Our detailed fieldwork, stratigraphic, biostratigraphic, petrographic, and geochemical investigations of the western part of Durkan Complex allow us to define in detail the nature of its

forming tectonic slices, as well as to suggest a tectonic model of formation, which significantly differs from those so far proposed in literature. The main conclusions of this work are then summarized as follows.

(1) The Durkan Complex in the western North Makran consists of several fault-bounded slices in which different stratigraphic successions can be recognized, though showing polyphase folding and thrusting deformation.
(2) Stratigraphic observations in the different slices allow us to recognize three types of successions. Type-I consists of a pelagic sequence in which pillow lava flows, pillow breccias, and volcaniclastic arenites are interbedded. Type-II is characterized by a volcanic sequence passing upward to a volcano-sedimentary sequence, as well as by the distinctive occurrence of abundant mass-transport deposits consisting of volcaniclastic and/or carbonatic arenites and breccias. Type-III succession includes a volcanic sequence and volcano-sedimentary sequence, passing upward to a shallow-water carbonatic platfrom succession. Significantly, all the successions lack continental-derived debris within the clastic deposits.
(3) Foraminifera, calcareous nannofossils, and radiolarian biostratigraphic data show that the volcanic rocks in Type-I and Type-II successions are associated with Coniacian – early Campanian sedimentary rocks and Cenomanian pelagic limestone, respectively. The carbonatic platform overlaying the volcanic and volcano-sedimentary sequence in Type-III succession is Cenomanian in age. (4) Volcanic rocks in all the succession types consist of basalts showing alkaline geochemical affinity, which point out for an oceanic within-plate setting of formation. A comparative study of the vesicles contents per volume show that from Type-I to Type-III successions the volcanic rocks were most likely erupted at progressively shallow depths.
(4) Volcanic rocks in all the succession types consist of basalts showing alkaline geochemical affinity, which point out for an oceanic within-plate setting of formation. A comparative study of the vesicles contents per volume show that from Type-I to Type-III successions the volcanic rocks were most likely erupted at progressively shallow depths.

Our data indicate that the western Durkan Complex successions have recorded complex Late Cretaceous interplay of sedimentation and alkaline magmatism, which is significantly younger than the Middle Jurassic – Early Cretaceous rifting stages recognized in literature in the eastern Durkan Complex. Therefore, we suggest that the western Durkan Complex represents tectonically disrupted portions of seamounts formed during Late Cretaceous in the northern sector of the Neo-Tethys realm. Finally, the incorporation of the Durkan seamounts in the Makran Accretionary Prism likely occurred during the latest Late Cretaceous–Paleocene and represents a major tectonic event, which likely caused an internal structural reorganization of the whole Makran convergent margin influencing its deformation style.

Supplementary data to this article can be found online at https://doi.org/10.1016/j.gsf.2020.12.001.

Declaration of Competing Interest

The authors declare that they have no known competing financial interests or personal relationships that could have appeared to influence the work reported in this paper.

Acknowledgments

The research has been funded by Darius Project (Head M. Marroni), as well as by the PRA project of the Pisa University (Head S. Rocchi), grants from IGG-CNR, and FAR-2018 Project of the Ferrara University (Head E.S. and V.L.). R. Tassinari and R. Tamoni (University of Ferrara) are acknowledged for technical support with chemical analyses and with thin section production, respectively. Thanks go to Špela Goričan for her useful suggestions. Mr. Ahmad Behboodi is sincerely thanked for his appreciated assistance in organizing field work, and PhD student Ahmad Nateghpour from Kharazmi University is thanked for his help during field work. Constructive and thorough reviews for the journal by three anonymous reviewers, as well as valuable suggestions by the Associate Editor I. Safonova and the Editorial Advisor M. Santosh have helped us improve the science and organization presented in the paper.

References

Afghah, M., Yousefzadeh, A., Shirdel, S., 2014. Biostratigraphic revision of Middle Cretaceous succession in South Zagros Basin (SW of Iran). J. Earth Sci. Clim. Change 5 (8), 1000216. https://doi.org/10.4172/2157-7617.1000216.

Agard, P., Omarani, J., Jolivet, L., Whitechurch, H., Vrielynck, B., Spakman, W., Monié, P., Meyer, B., Wortel, R., 2011. Zagros orogeny: a subduction-dominated process. Geol. Mag. 148, 692–725. https://doi.org/10.1017/S001675681100046X.

Azizi, H., Lucci, F., Stern, R.J., Hasannejad, S., Asahara, Y., 2018. The Late Jurassic Panjeh submarine volcano in the northern Sanandaj-Sirjan Zone, northwest Iran: mantle plume or active margin? Lithos 308–309, 364–380. https://doi.org/10.1016/j.lithos.2018.03.019.

Backman, J., Shackleton, N.J., 1983. Quantitative biochronology of Pliocene and Pleistocene calcareous nannofossils from the Atlanctic, Indian and Pacific oceans. Mar. Micropaleontol. 8, 141–170.

Bagheri, S., Stampfli, G., 2008. The Anarak, Jandaq and Posht-e-Badam metamorphic complexes in central Iran: new geological data, relationships and tectonic implications. Tectonophysics 451, 123–155. https://doi.org/10.1016/j.tecto.2007.11.047.

Barbero, E., Delavari, M., Dolati, A., Vahedi, L., Langone, A., Marroni, M., Pandolfi, L., Zaccarini, F., Saccani, E., 2020c. Early Cretaceous Plume–Ridge Interaction Recorded in the Band-e-Zeyarat Ophiolite (North Makran, Iran): New Constraints from Petrological. Mineral Chemistry, and Geochronological Data. Minerals 10, 1100. https://doi.org/10.3390/min10121100.

Barbero, E., Festa, A., Saccani, E., Catanzariti, R., D'Onofrio, R., 2020a. Redefinition of the Ligurian Units at the Alps–Apennines junction (NW Italy) and their role in the evolution of the Ligurian accretionary wedge: constraints from mélanges and broken formations. J. Geol. Soc. 177 (3), 562–574. https://doi.org/10.1144/jgs2019-022.

Bangs, N.L.B., Gulick, S.P.S., Shipley, T.H., 2006. Seamount subduction erosion in the Nankai Trough and its potential impact on the seismogenic zone. Geology 34, 701–704. https://doi.org/10.1130/G22451.1.

Barbero, E., Delavari, M., Dolati, A., Saccani, E., Marroni, M., Catanzariti, R., Pandolfi, L., 2020b. The Ganj Complex reinterpreted as a Late Cretaceous volcanic arc: implications for the geodynamic evolution of the North Makran domain (southeast Iran). J. Asia Earth Sci. https://doi.org/10.1016/j.jseaes.2020.104306.

Zanchetta, S., Berra, F., Zanchi, A., Bergomi, M., Caridroit, M., Nicora, A., Heidarzadeh, G., 2013. The record of the Late Palaeozoic active margin of the Palaeotethys in NE Iran: Constraints on the Cimmerian orogeny. Gondwana Res. 24, 1237–1266. https://doi.org/10.1016/j.gr.2013.02.013.

Barrier, E., Vrielynck, B., Brouillet, J.F., Brunet, M.F., 2018. Paleotectonic Reconstruction of the Central Tethyan Realm. Tectonono-Sedimentary-Palinspastic maps from Late Permian to Pliocene. Atlas of 20 maps (scale: 1:15.000.000). CCGM/CGMW, Paris, http://www.ccgm.org.

Berra, F., Galli, M.T., Reghellin, F., Torricelli, S., Fantoni, R., 2009. Stratigraphic evolution of the Triassic-Jurassic succession in the Western Southern Alps (Italy): the record of the two-stage rifting on the distal passive margin of Adria. Basin Res. 21 (3), 335–353. https://doi.org/10.1111/j.1365-2117.2008.00384.x.

Bonnet, G., Agard, P., Angiboust, S., Monié, P., Fournier, M., Caron, B., Omrani, J., 2020a. Structure and metamorphism of a subducted seamount (Zagros suture, Southern Iran). Geosphere 16, 62–81. https://doi.org/10.1130/GES02134.1.

Bonnet, G., Agard, P., Whitechurch, H., Fournier, M., Angiboust, S., Caron, B., Omrani, J., 2020b. Fossil seamount in southeast Zagros records intraoceanic arc to back-arc transition: New constraints for the evolution of the Neotethys. Gondwana Res. 81, 423–444. https://doi.org/10.1016/j.gr.2019.10.019.

Bown, P.R., Young, J.R., 1998. Techniques. In: Bown, P.R. (Ed.), Calcareous Nannofossil Biostratigraphy. British Micropalaeontology Society Publication Series. Kluwer Academic Publishers, Dordrecht, pp. 16–28.

Burg, J.-P., 2018. Geology of the onshore Makran accretionary wedge: synthesis and tectonic interpretation. Earth Sci. Rev. 185, 1210–1231. https://doi.org/10.1016/j.earscirev.2018.09.011.

Burg, J.-P., Bernoulli, D., Smit, J., Dolati, A., Bahroudi, A., 2008. A giant catastrophic mud-and-debris flow in the Miocene Makran. Terra Nova 20, 188–193. https://doi.org/10.1111/j.1365-3121.2008.00804.x.

Burg, J.-P., Dolati, A., Bernoulli, D., Smit, J., 2013. Structural style of the Makran tertiary accretionary complex in SE Iran. In: Al Hosani, K., Roure, F., Ellison, R., Lokier, S. (Eds.), Lithosphere Dynamics and Sedimentary Basins: The Arabian Plate and Analogues. Frontiers in Earth Sciences. Springer, Heidelberg, pp. 239–259 https://doi.org/10.1007/978-3-642-30609-9_12.

Cann, J.R., 1970. Rb, Sr, Y, Zr and Nb in some ocean floor basaltic rocks. Earth Planet. Sci. Lett. 10, 7–11.

Charvet, J., Ogawa, Y., 1994. Arc-trench tectonic. In: Hancock, P.L. (Ed.), Continental Deformation. Pergamon Press, Oxford, pp. 180–199.
Clarke, A.P., Vannucchi, P., Morgan, J., 2018. Seamount chain–subduction zone interactions: implications for accretionary and erosive subduction zone behavior. Geology 46, 367–370. https://doi.org/10.1130/G40063.1.
Clift, P., Vannucchi, P., 2004. Controls on tectonic accretion versus erosion in subduction zones: Implications for the origin and recycling of the continental crust. Rev. Geophys. 42 (2), RG2001. https://doi.org/10.1029/2003RG000127.
Cloos, M., 1993. Lithospheric buoyancy and collisional orogenesis: Subduction of oceanic plateaus, continental margins, island arcs, spreading ridges, and seamounts. Geol. Soc. Am. Bull. 105, 715–737. https://doi.org/10.1130/0016-7606(1993)105<0715:LBACOS>2.3.CO;2.
Coccioni, R., Premoli Silva, I., 2015. Revised Upper Albian-Maastrichtinan planktic foraminiferal biostratigraphy and magnetostratigraphy of the classical Tethyan Gubbio section (Italy). Newsl. Stratigr. 48 (1), 47–90.
Corcoran, P.L., 2000. Recognizing distinct portions of seamounts using volcanic facies analysis: examples from the Archean Slave Province, NWT, Canada. Precambrian Res. 101, 237–261. https://doi.org/10.1016/S0301-9268(99)00090-X.
Davis, D., Suppe, J., Dahlen, F.A., 1983. Mechanics of fold-and-thrust belts and accretionary wedges. J. Geophys. Res. 88 (B12), 1153–1172. https://doi.org/10.1029/JB088iB02p01153.
Delaloye, M., Desmons, J., 1980. Ophiolites and mélange terranes in Iran: A geochronological study and its paleotectonic implications. Tectonophysics 68, 83–111.
Delavari, M., Dolati, A., Marroni, M., Pandolfi, L., Saccani, E., 2016. Association of MORB and SSZ ophiolites along the shear zone between Coloured Mélange and Bajgan Complexes (North Maran, Iran): evidence from the Sorkhband area. Ofioliti 41, 21–34. https://doi.org/10.4454/ofioliti.v41i1.440.
Dercourt, J., Zonenshian, L.P., Ricou, L.E., Kazmin, V.G., LePichon, X., Knipper, A.L., Grandjacquet, C., Sbortshikov, M., Geyssant, J., Lepvrier, C., Pechersky, D.H., Boulin, J., Sibuet, J.C., Savostin, L.A., Sorokhtin, O., Westphal, M., Bazhenov, M.L., Lauer, J.P., Biju-Duval, B., 1986. Geological evolution of the Tethys Belt from the Atlantic to the Pamir since the Lias. Tectonophysics 123, 241–315.
Desmons, J., Beccaluva, L., 1983. Mid-Ocean ridge and island-arc affinities in ophiolites from Iran: Palaeographic implications. Chem. Geol. 39, 39–63.
Dilek, Y., Furnes, H., 2011. Ophiolite genesis and global tectonics: geochemical and tectonic fingerprinting of ancient oceanic lithosphere. Geol. Soc. Am. Bull. 123, 387–411. https://doi.org/10.1130/B30446.1.
Dolati, A., 2010. Stratigraphy, Structure Geology and Low-temperature Thermochronology Across the Makran Accretionary Wedge in Iran. PhD thesis, ETH Zurich, 165 pp.
Dolati, A., Burg, J.-P., 2013. Preliminary fault analysis and paleostress evolution in the Makran Fold-and-Thrust Belt in Iran. In: Al Hosani, K., Roure, F., Ellison, R., Lokier, S. (Eds.), Lithosphere Dynamics and Sedimentary Basins: The Arabian Plate and Analogues. Frontiers in Earth Sciences, Springer, Heidelberg, pp. 261–277 https://doi.org/10.1007/978-3-642-30609-9_13.
Dominguez, S., Lallemand, S.E., Malavieille, J., von Huene, R., 1998. Upper plate deformation associated with seamount subduction. Tectonophysics 293, 207–224. https://doi.org/10.1016/S0040-1951(98)00086-9.
Dorani, M., Arvin, M., Oberhänsli, R., Dargahi, S., 2017. P-T evolution of metapelites from the Bajgan complex in the Makran accretionary prism, south eastern Iran. Geochemistry 77, 459–475. https://doi.org/10.1016/j.chemer.2017.07.004.
Eftekhar-Nezhad, J., Arshadi, S., Mahdavi, M.A., Morgan, K.H., McCall, G.J.H., Huber, H., 1979. Fannuj Quadrangle Map 1:250000. Ministry of Mines and Metal, Geological Survey of Iran, Tehran.
Engdahl, E., Jackson, J.A., Myers, S.C., Bergman, E.A., Priestley, K., 2006. Relocation and assessment of seismicity in the Iran region. Geophys. J. Int. 167 (2), 761–778. https://doi.org/10.1111/j.1365-246X.2006.03127.x.
Entezar-Saadat, V., Motavalli-Anbaran, S.H., Zeyen, H., 2017. Lithospheric structure of the Eastern Iranian plateau from integrated geophysical modeling: a transect from Makran to the Turan platform. J. Asian Earth Sci. 138, 357–366. https://doi.org/10.1016/j.jseaes.2017.02.024.
Esmaeili, R., Xiao, W., Ebrahimi, M., Zhang, J., Zhang, Z., Abd El-Rahman, Y., Han, C., Wan, B., Ao, S., Song, D., Shahabi, S., Aouizerat, A., 2019. Makran ophiolitic basalts (SE Iran) record Late Cretaceous Neotethys plume-ridge interaction. Int. Geol. Rev., 1–21 https://doi.org/10.1080/00206814.2019.1658232.
Esmaeili, R., Xiao, W., Griffin, W.L., Moghadam, H.S., Zhang, Z., Ebrahimi, M., Zhang, J., Wan, B., Ao, S., Bhandari, S., 2020. Reconstructing the source and growth of the Makran Accretionary Complex: constraints from detrital zircon U-Pb geochronology. Tectonics 39 (2). https://doi.org/10.1029/2019TC005963.
Festa, A., Dilek, Y., Mittempergher, S., Ogata, K., Pini, G.A., Remitti, F., 2018. Does subduction of mass transport deposits (MTDs) control seismic behavior of shallow–level megathrusts at convergent margins? Gondwana Res. 60, 186–193. https://doi.org/10.1016/j.gr.2018.05.002.
Festa, A., Balestro, G., Borghi, A., De Caroli, S., Succo, A., 2020. The role of structural inheritance in continental break-up and exhumation of Alpine Tethyan mantle (Canavese Zone, Western Alps). Geosci. Front. 11 (1), 167–188. https://doi.org/10.1016/j.gsf.2018.11.007.
Fisher, R.V., 1984. Submarine volcaniclastic rocks. Geol. Soc. Lond. Spec. Publ. 16 (1), 5–27. https://doi.org/10.1144/GSL.SP.1984.016.01.02.
Foreman, H.P., 1977. Mesozoic radiolaria from the Atlantic Basin and its borderlands. In: Swain, F.M. (Ed.), Stratigraphic Micropaleontology of the Atlantic Basin and Borderlands. Elsevier, pp. 305–320.
Gansser, A., 1955. New aspects of the geology in central Iran. 4th World Petroleum Congress, Rome, Italy, pp. 279–300.
Ghazi, A.M., Hassanipak, A.A., Mahoney, J.J., Duncon, R.A., 2004. Geochemical characteristics, ^{40}Ar-^{39}Ar ages and original tectonic setting of the Band-e-Zeyarat/Dar Anar ophiolite, Makran accretionary Prism, S.E. Iran. Tectonophysics 193, 175–196. https://doi.org/10.1144/GSL.SP.1984.016.01.02.
Glennie, K.W., Hughes Clarke, M.W., Boeuf, M.G.A., Pilaar, W.F.H., Reinhardt, B.M., 1990. Inter-relationship of Makran-Oman Mountains belts of convergence. Geol. Soc. Lond. Spec. Publ. 49, 773–786. https://doi.org/10.1144/GSL.SP.1992.049.01.47.
Gradstein, F.M., Ogg, J.G., Scmitz, M.D., Ogg, G.M., 2012. The Geologic Time Scheme. International Commission on Stratigraphy. Elsevier, Amsterdam, p. 1144.
Grando, G., McClay, K., 2007. Morphotectonics domains and structural styles in the Makran accretionary prism, offshore Iran. Sediment. Geol. 196, 157–179. https://doi.org/10.1016/j.sedgeo.2006.05.030.
Gutierrez, M., Casillas, R., Fernandez, C., Balogh, K., Ahijado, A., Castillo, C., Colmenero, J.R., Garcia-Navarro, E., 2006. The submarine volcanic succession of the basal complex of Fuerteventura, Canary Islands: a model of submarine growth and emergence of tectonic volcanic islands. Geol. Soc. Am. Bull. 118, 785–804. https://doi.org/10.1130/B25821.1.
Hassanzadeh, J., Wernicke, B.P., 2016. The Neotethyan Sanandaj-Sirjan zone of Iran as an archetype for passive margin-arc transitions. Tectonics 35, 586–621. https://doi.org/10.1002/2015TC003926.
Hässig, M., Rolland, Y., Sosson, M., Galoyan, G., Müller, C., Avagyan, A., Sahakyan, L., 2013a. New structural and petrological data on the Amasia ophiolites (NW Sevan–Akera suture zone, Lesser Caucasus): insights for a large-scale obduction in Armenia and NE Turkey. Tectonophysics 588, 135–153. https://doi.org/10.1016/j.tecto.2012.12.003.
Hässig, M., Rolland, Y., Sosson, M., Galoyan, G., Sahakyan, L., Topuz, G., Çelik, Ö.F., Avagyan, A., Müller, C., 2013b. Linking the NE Anatolian and Lesser Caucasus ophiolites: evidence for large-scale obduction of oceanic crust and implications for the formation of the Lesser Caucasus-Pontides Arc. Geodin. Acta 26, 311–330. https://doi.org/10.1080/09853111.2013.877236.
Hunziker, D., 2014. Magmatic and Metamorphic History of the North Makran Ophiolites and Blueschists (SE Iran): Influence of Fe^{3+}/Fe^{2+} Ratios in Blueschist Facies Minerals on Geothermobarometric Calculations. Ph.D thesis. ETH Zurich, Switzerland, p. 364.
Hunziker, D., Burg, J.-P., Bouilhol, P., von Quadt, A., 2015. Jurassic rifting at the Eurasian Tethys margin: Geochemical and geochronological constraints from granitoids of North Makran, southeastern Iran. Tectonics 34, 571–593. https://doi.org/10.1002/2014TC003768.
Isozaki, Y., 1997. Contrasting two types of orogen in Permo-Triassic Japan: accretionary versus collisional. Island Arc 6, 2–24. https://doi.org/10.1111/j.1440-1738.1997.tb00038.x.
Isozaki, Y., Maruyama, S., Furuoka, F., 1990. Accreted oceanic materials in Japan. Tectonophysics 181, 179–205. https://doi.org/10.1016/0040-1951(90)90016-2.
Janney, P.E., Le Roex, A.P., Carlson, R.L., 2005. Hafnium isotope and trace element constraints on the nature of mantle heterogeneity beneath the Central Southwest Indian Ridge. J. Petrol. 46, 2427–2464.
Kananian, A., Juteau, T., Bellon, H., Darvishzadeh, A., Sabzehi, M., Whitechurch, H., Ricou, L.-E., 2001. The ophiolite massif of Kahnuj (western Makran, southern Iran): new geological and geochronological data. C. R. Acad. Sci. Ser. IIA Earth Planet. Sci. 332, 543–552.
Kerr, A.C., 2014. Oceanic plateaus. In: Holland, H.D., Turekian, K.K. (Eds.), Treatise on Geochemistry. Elsevier, Oxford, pp. 631–667.
Kopp, C., Fruehn, J., Flueh, E.R., Reichert, C., Kukowski, N., Bialas, J., Klaeschen, D., 2000. Structure of the Makran subduction zone from wide-angle and reflection seismic data. Tectonophysics 329, 171–191. https://doi.org/10.1016/S0040-1951(00)00195-5.
Kusky, T.M., Windley, B.F., Safonova, I., Wakita, K., Wakabayashi, J., Polat, A., Santosh, M., 2013. Recognition of ocean plate stratigraphy in accretionary orogens through Earth history: a record of 3.8 billion years of sea floor spreading, subduction, and accretion. Gondwana Res. 24, 501–547. https://doi.org/10.1016/j.gr.2013.01.004.
Lallemand, S., Le-Pichon, X., 1987. Coulomb wedge model applied to the subduction of seamounts in the Japan Trench. Geology 15 (11), 1065–1069.
Lallemand, S., Culotta, R., Von Huene, R., 1989. Subduction of the Daiichi Kashima seamount in the Japan Trench. Tectonophysics 160, 231–247.
Loeblich, A., Tappan, H., 1988. Foraminiferal General and Their Classification. vol. 2. Van Nostrand Reinhold, New York, p. 213.
MacPherson, G.T., 1983. The Snow Mountain Volcanic Complex: an on-land seamount in the Franciscan Terrain, California. J. Geol. 91, 73–92. https://doi.org/10.1086/628745.
Malatesta, C., Gerya, T., Crispini, L., Federico, L., Capponi, G., 2013. Oblique subduction modelling indicates along-trench tectonic transport of sediments. Nat. Commun. 4 (1), 2456. https://doi.org/10.1038/ncomms3456.
Marroni, M., Pandolfi, L., 2001. Debris flow and slide deposits at the top of the Internal Liguride ophiolitic sequence, Northern Apennines, Italy: a record of frontal tectonic erosion in a fossil accretionary wedge. Island Arc 10 (1), 9–21. https://doi.org/10.1046/j.1440-1738.2001.00289.x.
McCall, G.J.H., 1983. Mélanges of the Makran, southeastern Iran. In: McCall, G.J.H. (Ed.), Ophiolitic and Related Mélanges, Benchmark Papers in Geology. vol. 66. Hutchinson Ross Publishing Company, Stroudsburg, Pennsylvania, pp. 292–299.
McCall, G.J.H., 1985. Explanatory Text of the Minab Quadrangle Map; 1:250,000; No. J13. Geological Survey of Iran, Tehran, p. 530.
McCall, G.J.H., 1997. The geotectonic history of the Makran and adjacent areas of southern Iran. J. Asian Earth Sci. 15, 517–531.
McCall, G.J.H., 2002. A summary of the geology of the Iranian Makran. In: Clift, P.D., Kroon, F.D., Gaedecke, C., Craig, J. (Eds.), The Tectonic and Climatic Evolution of the Arabian Sea Region. vol. 195. Geol. Soc. Lond. Spec. Publ., pp. 147–204.
McCall, G.J.H., Kidd, R.G.W., 1982. The Makran southeastern Iran: the anatomy of a convergent margin active from Cretaceous to present. In: Leggett, J.K. (Ed.), Trench-forearc Geology: Sedimentation and Tectonics of Modern and Ancient Plate Margins. vol. 10. Geol. Soc. Lond. Spec. Publ., pp. 387–397.

McPhie, J., Doyle, M., Allen, R., 1993. Volcanic Textures: A Guide to the Interpretation of Textures in Volcanic Rocks. Hobart, Centre for Ore Deposit and Exploration Studies, University of Tasmania, Tasmanian Government Printing Office, p. 198.

Memtimin, M., Zhang, Y., Furnes, H., Pe-Piper, G., Piper, D.J.W., Guo, Z., 2019. Facies architecture of a subaqueous volcano–sedimentary succession on Bogda Mountains, NW China—evidence of extension in Late Carboniferous. Geol. J. 55 (4), 3097–3111. https://doi.org/10.1002/gj.3582.

Meneghini, F., Marroni, M., Moore, J.C., Pandolfi, L., Rowe, C.D., 2009. The processes of underthrusting and underplating in the geologic record: structural diversity between the Franciscan Complex (California), the Kodiak Complex (Alaska) and the Internal Ligurian Units (Italy). Geol. J. 44 (2), 126–152.

Mohammadi, A., Burg, J.-P., Winkler, W., Ruh, J., von Quadt, A., 2016. Detrital zircon and provenance analysis of Late Cretaceous–Miocene onshore Iranian Makran strata: Implications for the tectonic setting. Geol. Soc. Am. Bull. 128, 1481–1499. https://doi.org/10.1130/B31361.1.

Monsef, I., Rahgoshay, M., Pirouz, M., Chiaradia, M., Grégoire, M., Ceuleneer, G., 2019. The Eastern Makran Ophiolite (SE Iran): evidence for a Late Cretaceous fore-arc oceanic crust. Int. Geol. Rev. 61 (11), 1313–1339. https://doi.org/10.1080/00206814.2018.1507764.

Moore, J.G., 1970. Water Content of Basalt Erupted on the ocean floor. Contrib. Mineral. Petrol. 28 (4), 272–279. https://doi.org/10.1007/BF00388949.

Moore, J.G., Clague, D.A., 1992. Volcano growth and evolution of the island of Hawaii. Geol. Soc. Am. Bull. 104 (11), 1471–1484. https://doi.org/10.1130/0016-7606(1992)104<1471:VGAEOT>2.3.CO;2.

Moore, J.G., Schilling, J.G., 1973. Vesicles, water, and sulfur in Reykjanes Ridge basalts. Contrib. Mineral. Petrol. 41 (2), 105–118. https://doi.org/10.1007/BF00375036.

Moore, G.F., Shipley, T.H., Stoffa, P.L., Karig, D.E., Taira, A., Kuramoto, S., Tokuyama, H., Suyehiro, K., 1990. Structure of the Nankai Trough accretionary zone from multichannel seismic reflection data. J. Geophys. Res. Solid Earth 95, 8753–8765. https://doi.org/10.1029/JB095iB06p08753.

Morgan, W.J., 1971. Convection Plumes in the Lower Mantle. Nature 230, 42–43. https://doi.org/10.1038/230042a0.

Moslempour, M.E., Khalatbari-Jafari, M., Ghaderi, M., Yousefi, H., Shahdadi, S., 2015. Petrology, geochemistry and tectonics of the extrusive sequence of Fannuj-Maskutan Ophiolite, southeastern Iran. J. Geol. Soc. India 85, 604–618.

Motaghi, K., Shabanian, E., Nozad-Khalil, T., 2020. Deep structure of the western coast of the Makran subduction zone, SE Iran. Tectonophysics 776, 228314. https://doi.org/10.1016/j.tecto.2019.228314.

O'Dogherty, L., 1994. Biochronology and Paleontology of Mid-Cretaceous radiolarians from Northern Apennines (Italy) and Betic Cordillera (Spain). Mémoir. Géol. (Lausanne) 21, 1–413.

Omrani, H., Moazzen, M., Oberhänsli, R., Moslempour, M.E., 2017. Iranshahr blueschist: subduction of the inner Makran oceanic crust. J. Metamorph. Geol. 35, 373–392. https://doi.org/10.1111/jmg.12236.

Pearce, J.A., 1996. A user's guide to basalt discrimination diagrams. In: Bailes, A.H., Christiansen, E.H., Galley, A.G., Jenner, G.A., Keith, J.D., Kerrich, R., Wyman, D.A. (Eds.), Trace element geochemistry of volcanic rocks: applications for massive sulphide exploration. Short Course Notes. Geol. Assoc. Canada 12, pp. 79–113.

Pearce, J.A., 2008. Geochemical fingerprinting of oceanic basalts with applications to ophiolite classification and the search for Archean oceanic crust. Lithos 100, 14–48. https://doi.org/10.1016/j.lithos.2007.06.016.

Pearce, J.A., Norry, M.J., 1979. Petrogenetic implications of Ti, Zr, Y, and Nb variations in volcanic rocks. Contrib. Mineral. Petrol. 69, 33–47.

Penney, C., Copley, A., Oveisi, B., 2015. Subduction tractions and vertical axis rotations in the Zagros–Makran transition zone, SE Iran: the 2013 May 11 Mw 6.1 Minab earthquake. Geophys. J. Int. 202, 1122–1136. https://doi.org/10.1093/gji/ggv202.

Penney, C., Tavakoli, F., Saadat, A., Nankali, H.R., Sedighi, M., Khorrami, F., Sobouti, F., Rafi, Z., Copley, A., Jackson, J., Priestley, K., 2017. Megathrust and accretionary wedge properties and behaviour in the Makran subduction zone. Geophys. J. Int. 209, 1800–1830. https://doi.org/10.1093/gji/ggx126.

Pirnia, T., Saccani, E., Torabi, G., Chiari, M., Gorican, S., Barbero, E., 2020. Cretaceous tectonic evolution of the Neo-Tethys in Central Iran: evidence from petrology and age of the Nain-Ashin ophiolitic basalts. Geosci. Front. 11 (1), 57–81. https://doi.org/10.1016/j.gsf.2019.02.008.

Platt, J.P., Leggett, J.K., Young, J., Raza, H., Alam, S., 1985. Large-scale sediment underplating in the Makran accretionary prism, southwest Pakistan. Geology 13, 507. https://doi.org/10.1130/0091-7613(1985)13<507:LSUITM>2.0.CO;2.

Quartau, R., Ramalho, R.S., Madeira, J., Santos, R., Rodrigues, A., Roque, C., Carrara, G., Brum da Silveira, A., 2018. Gravitational, erosional and depositional processes on volcanic ocean islands: insights from the submarine morphology of Madeira Archipelago. Earth Planet. Sci. Lett. 482, 288–299. https://doi.org/10.1016/j.epsl.2017.11.003.

Ranero, C.R., von Huene, R., 2000. Subduction erosion along the Middle America convergent margin. Nature 404 (6779), 748–752. https://doi.org/10.1038/35008046.

Regard, V., Hatzfeld, D., Molinaro, M., Aubourg, C., Bayer, R., Bellier, O., Yamini-Fard, F., Peyret, M., Abbassi, M., 2010. The transition between Makran subduction and the Zagros collision: recent advances in its structure and active deformation. Geol. Soc. Lond. Spec. Publ. 330 (1), 43–64. https://doi.org/10.1144/SP330.4.

Riaz, M.S., Bin, S., Naeem, S., Kai, W., Xie, Z., Gilani, S.M.M., Ashraf, U., 2019. Over 100 years of faults interaction, stress accumulation, and creeping implications, on Chaman Fault System, Pakistan. Int. J. Earth Sci. 108 (4), 1351–1359. https://doi.org/10.1007/s00531-019-01710-0.

Ricou, L.E., 1994. Tethys reconstructed: plates continental fragments and their boundaris since 260 Ma from Central America to South-eastern Asia. Geodin. Acta 7, 169–218.

Riedel, W.R., Sanfilippo, A., 1974. 33. Radiolaria from the southern Indian Ocean, DSDP leg 26. In: Davis, T.A., Luyendyke, B.P. (Eds.), Initial Reports of the Deep Sea Drilling Project. 26. U. S. Goverment Printing Office, Washington, pp. 771–783.

Robertson, A.H.F., 2007. Overview of tectonic settings related to the rifting and opening of Mesozoic ocean basins in the Eastern Tethys: Oman, Himalayas and Eastern Mediterranean regions. Geol. Soc. Lond. Spec. Publ. 282, 325–388. https://doi.org/10.1144/SP282.15.

Rolland, Y., Galoyan, G., Sosson, M., Melkonyan, R., Avagyan, A., 2010. The Armenian Ophiolite: insights for Jurassic back-arc formation, Lower Cretaceous hot spot magmatism and Upper Cretaceous obduction over the South Armenian Block. Geol. Soc. Lond. Spec. Publ. 340, 353–382. https://doi.org/10.1144/SP340.15.

Rolland, Y., Hässig, M., Bosch, D., Bruguier, O., Melis, R., Galoyan, G., Topuz, G., Sahakyan, L., Avagyan, A., Sosson, M., 2020. The East Anatolia–Lesser Caucasus ophiolite: an exceptional case of large-scale obduction, synthesis of data and numerical modelling. Geosci. Front. 11 (1), 83–108. https://doi.org/10.1016/j.gsf.2018.12.009.

Ruh, J.B., 2016. Submarine landslides caused by seamounts entering accretionary wedge systems. Terra Nova 28 (3), 163–170. https://doi.org/10.1111/ter.12204.

Saccani, E., 2015. A new method of discriminating different types of post-Archean ophiolitic basalts and their tectonic significance using Th-Nb and Ce-Dy-Yb systematics. Geosci. Front. 6 (4), 481–501. https://doi.org/10.1016/j.gsf.2014.03.006.

Saccani, E., Allahyari, K., Beccaluva, L., Bianchini, G., 2013. Geochemistry and petrology of the Kermanshah ophiolites (Iran): Implication for the interaction between passive rifting, oceanic accretion, and OIB-type components in the Southern Neo-Tethys Ocean. Gondwana Res. 24, 392–411. https://doi.org/10.1016/j.gr.2012.10.009.

Saccani, E., Dilek, Y., Marroni, M., Pandolfi, L., 2015. Continental margin ophiolites of Neotethys: remnants of Ancient Ocean–Continent Transition Zone (OCTZ) lithosphere and their geochemistry, mantle sources and melt evolution patterns. Episodes 38, 230–249. https://doi.org/10.18814/epiiugs/2015/v38i4/82418.

Saccani, E., Delavari, M., Dolati, A., Marroni, M., Pandolfi, L., Chiari, M., Barbero, E., 2018. New insights into the geodynamics of Neo-Tethys in the Makran area: evidence from age and petrology of ophiolites from the Coloured Mélange Complex (SE Iran). Gondwana Res. 62, 306–327. https://doi.org/10.1016/j.gr.2017.07.013.

Safonova, I.Y., Santosh, M., 2014. Accretionary complexes in the Asia-Pacific region: tracing archives of ocean plate stratigraphy and tracking mantle plumes. Gondwana Res. 25, 126–158. https://doi.org/10.1016/j.gr.2012.10.008.

Safonova, I., Maruyama, S., Kojima, S., Komiya, T., Krivonogov, S., Koshida, K., 2016. Recognizing OIB and MORB in accretionary complexes: a new approach based on ocean plate stratigraphy, petrology and geochemistry. Gondwana Res. 33, 92–114. https://doi.org/10.1016/j.gr.2015.06.013.

Saint-Ange, F., Bachèlery, P., Babonneau, N., Michon, L., Jorry, S.J., 2013. Volcaniclastic sedimentation on the submarine slopes of a basaltic hotspot volcano: Piton de la Fournaise volcano (La Réunion Island, Indian Ocean). Mar. Geol. 337, 35–52. https://doi.org/10.1016/j.margeo.2013.01.004.

Samimi Namin, M., 1982. Geological Map of Taherui 1:250000 Scale. Ministry of Mines and Metal, Geological Survey of Iran, Tehran.

Samimi Namin, M., 1983. Geological Map of Minab 1:250000 Scale. Ministry of Mines and Metal, Geological Survey of Iran, Tehran.

Sanfilippo, A., Riedel, W.R., 1985. Cretaceous radiolaria. In: Bollli, H.M., Saunders, J.B., Perch-Nielson, K. (Eds.), Plankton Stratigraphy. Cambridge University Press, pp. 573–630.

Schlanger, S.O., Jenkyns, H.C., 1976. Cretaceous oceanic anoxic events: causes and consequences. Geol. Mijnb. 55, 179–184.

Schnur, S.R., Gilbert, L.A., 2012. Detailed volcanostratigraphy of an accreted seamount: implications for intraplate seamount formation. Geochem. Geophys. Geosyst. 13, 1–13. https://doi.org/10.1029/2012GC004301.

Şengör, A.M.C., Altıner, D., Cin, A., Ustaömer, T., Hsü, K.J., 1988. Origin and assembly of the Tethyside orogenic collage at the expense of Gondwana Land. Geol. Soc. Lond. Spec. Publ. 37, 119–181. https://doi.org/10.1144/GSL.SP.1988.037.01.09.

Sepidbar, F., Lucci, F., Biabangard, H., Zaki Khedr, M., Jiantang, P., 2020. Geochemistry and tectonic significance of the Fannuj-Maskutan SSZ-type ophiolite (Inner Makran, SE Iran). Int. Geol. Rev., 2077–2104 https://doi.org/10.1080/00206814.2020.1753118.

Shervais, J.W., 1982. Ti-V plots and the petrogenesis of modern and ophiolitic lavas. Earth Planet. Sci. Lett. 59, 101–118. https://doi.org/10.1016/0012-821X(82)90120-0.

Shervais, J.W., Schuman Zoglman, M.M., Hanan, B.B., 2005. The Stonyford Volcanic Complex: a forearc seamount in the Northern California coast ranges. J. Petrol. 46, 2091–2128. https://doi.org/10.1093/petrology/egi048.

Staudigel, H., Clague, D.A., 2010. The geological history of deep-sea volcanoes: Biosphere, hydrosphere, and lithosphere interactions. Oceanography 23, 58–71. https://doi.org/10.2307/24861062.

Staudigel, H., Schmincke, H.-U., 1984. The Pliocene seamount series of La Palma/Canary Islands. J. Geophys. Res. Solid Earth 89 (B13), 11195–11215. https://doi.org/10.1029/JB089iB13p11195.

Stern, C.R., 2011. Subduction erosion: rates, mechanisms, and its role in arc magmatism and the evolution of the continental crust and mantle. Gondwana Res. 20 (2–3), 284–308. https://doi.org/10.1016/j.gr.2011.03.006.

Sun, S.S., McDonough, W.F., 1989. Chemical and isotopic systematics of oceanic basalts: implications for mantle composition and processes. In: Saunders, A.D., Norry, M.J. (Eds.), Magmatism in the Ocean Basins. vol. 42. Geol. Soc. Lond. Spec. Publ., pp. 313–345.

Vannucchi, P., Fisher, D.M., Bier, S., Gardner, T.W., 2006. From seamount accretion to tectonic erosion: formation of Osa Mélange and the effects of Cocos Ridge subduction in southern Costa Rica. Tectonics 25 (2), TC2004. https://doi.org/10.1029/2005TC001855.

von Huene, R., Lallemand, S., 1990. Tectonic erosion along the Japan and Peru convergent margins. Geol. Soc. Am. Bull. 102 (6), 704–720.

von Huene, R., Ranero, C.R., Vannucchi, P., 2004a. Generic model of subduction erosion. Geology 32, 913–916. https://doi.org/10.1130/G20563.1.

von Huene, R., Ranero, C.R., Watts, P., 2004b. Tsunamigenic slope failure along the Middle America Trench in two tectonic settings. Mar. Geol. 203, 303–317. https://doi.org/10.1016/S0025-3227(03)00312-8.

White, R.S., Klitgord, K., 1976. Sediment deformation and plate tectonics in the Gulf of Oman. Earth Planet. Sci. Lett. 32, 199–209. https://doi.org/10.1016/0012-821X(76)90059-5.

Winchester, J.A., Floyd, P.A., 1977. Geochemical discrimination of different magma series and their differentiation products using immobile elements. Chem. Geol. 20, 325–343.

Yang, G., Dilek, Y., 2015. OIB- and P-type ophiolites along the Yarlung- Zangbo Suture Zone (YZSZ), Southern Tibet: Poly-Phase melt history and mantle sources of the Neotethyan oceanic lithosphere. Episodes 38 (4), 250–265. https://doi.org/10.18814/epiiugs/2015/v38i4/82420.

Young, J.R., Bown, P.R., Lees, J.A., 2017. Nannotax3 website. International Nannoplankton Association. Accessed 21 Apr. 2017. URL: http://www.mikrotax.org/Nannotax3